AGU PUBLICATIONS

JGR

Journal of Geophysical Research: Atmospheres

RESEARCH ARTICLE

10.1002/2016JD025586

This article is a companion to *Yi et al.* [2017] doi:10.1002/2016JD025654.

Key Points:

- We compare differences in ice and liquid water cloud physical and optical properties between Aqua MODIS collection 6 and collection 5.1
- Significant differences between C6 and C51 cloud physical and optical properties are found
- The C6 radiative effects compare more closely with the CERES EBAF product than the C51 counterparts

Correspondence to:
B. Yi,
bingqi.yi@outlook.com

Citation:
Yi, B., A. D. Rapp, P. Yang, B. A. Baum, and M. D. King (2017), A comparison of Aqua MODIS ice and liquid water cloud physical and optical properties between collection 6 and collection 5.1: Pixel-to-pixel comparisons, *J. Geophys. Res. Atmos.*, *122*, 4528–4549, doi:10.1002/2016JD025586.

Received 28 JUN 2016
Accepted 31 MAR 2017
Accepted article online 7 APR 2017
Published online 29 APR 2017

A comparison of Aqua MODIS ice and liquid water cloud physical and optical properties between collection 6 and collection 5.1: Pixel-to-pixel comparisons

Bingqi Yi[1], Anita D. Rapp[1], Ping Yang[1], Bryan A. Baum[2], and Michael D. King[1,3]

[1]Department of Atmospheric Sciences, Texas A&M University, College Station, Texas, USA, [2]Space Science and Engineering Center, University of Wisconsin-Madison, Madison, Wisconsin, USA, [3]Laboratory for Atmospheric and Space Physics, University of Colorado Boulder, Boulder, Colorado, USA

Abstract We compare differences in ice and liquid water cloud physical and optical properties between Aqua Moderate Resolution Imaging Spectroradiometer (MODIS) collection 6 (C6) and collection 5.1 (C51). The C6 cloud products changed significantly due to improved calibration, improvements based on comparisons with the Cloud-Aerosol Lidar with Orthogonal Polarization, treatment of subpixel liquid water clouds, introduction of a roughened ice habit for C6 rather than the use of smooth ice particles in C51, and more. The MODIS cloud products form a long-term data set for analysis, modeling, and various purposes. Thus, it is important to understand the impact of the changes. Two cases are considered for C6 to C51 comparisons. Case 1 considers pixels with valid cloud retrievals in both C6 and C51, while case 2 compares all valid cloud retrievals in each collection. One year (2012) of level-2 MODIS cloud products are examined, including cloud effective radius (CER), optical thickness (COT), water path, cloud top pressure (CTP), cloud top temperature, and cloud fraction. Large C6–C51 differences are found in the ice CER (regionally, as large as 15 μm) and COT (decrease in annual average by approximately 25%). Liquid water clouds have higher CTP in marine stratocumulus regions in C6 but lower CTP globally (−5 hPa), and there are 66% more valid pixels in C6 (case 2) due to the treatment of pixels with subpixel clouds. Simulated total cloud radiative signatures from C51 and C6 are compared to Clouds and the Earth's Radiant Energy System Energy Balanced And Filled (EBAF) product. The C6 CREs compare more closely with the EBAF than the C51 counterparts.

1. Introduction

The spectral measurements provided by the Moderate Resolution Imaging Spectroradiometer (MODIS) instruments on board the NASA Earth Observing System Terra and Aqua satellites form the basis for a decadal cloud climatology, providing a link with cloud products from earlier sensors such as the Advanced Very High Resolution Radiometer [*Foster and Heidinger*, 2013] and the High-Resolution Infrared Radiometer Sounder [*Menzel et al.*, 2016] on the NOAA polar-orbiting platforms. The Aqua MODIS is part of the A-train satellite constellation and can be collocated with the other sensors such as the Cloud-Aerosol Lidar with Orthogonal Polarization (CALIOP) on the Cloud-Aerosol Lidar and Infrared Pathfinder Satellite Observations (CALIPSO) [*Winker et al.*, 2009] and CloudSat [i.e., *Stephens et al.*, 2008; *Delanoë and Hogan*, 2010]. Recently, a new collection of MODIS products (collection 6) became available to the community, with upgrades in the calibration [*Toller et al.*, 2013] and cloud top property retrieval algorithms [*Baum et al.*, 2012]. This was a significant upgrade from collection 5 (henceforth C5) for the primary reason that the CALIOP lidar products, e.g., cloud top height and cloud thermodynamic phase, were used extensively during the MODIS algorithm development and testing process. As the MODIS cloud products are used in so many different communities, it is important to understand the differences between the collection 5.1 (henceforth C51) and collection 6 (henceforth C6) products.

The MODIS cloud products have been used, for example, in studies of cloud radiation and cloud feedbacks [*Oreopoulos et al.*, 2014; *Zhou et al.*, 2013]. The radiative effect of clouds on the climate is related to their microphysical and optical properties [*Yang et al.*, 2007]. Properly representing clouds and cloud radiative effects within general circulation models (GCMs) has long been a great challenge [*Yi et al.*, 2013; *Jiang et al.*, 2012; *Waliser et al.*, 2009]. Now that multiple decadal global cloud property data sets are available [e.g., *Heidinger et al.*, 2014; *Stengel et al.*, 2014; *Menzel et al.*, 2016], with much improved radiometric calibration [e.g., *Heidinger et al.*, 2010], the modeling and satellite communities will be able to better compare global cloud characteristics. The goal of this study is to better understand the changes in the MODIS C6 cloud products because of the many advances in calibration [e.g., *Xiong et al*., 2009, 2016], retrieval methodology, ancillary data, and validation with CALIOP products. Such a study may lead to closer comparisons with GCM simulations and improvements in the cloud radiation modeling capabilities of GCMs.

Given the improvements implemented during each MODIS collection, changes in the cloud property retrievals are inevitable [*Yang et al*., 2007]. These changes are made for various reasons, including advances in the development of ice particle scattering and absorption properties [*Yang et al*., 2013; *Baum et al*., 2014], the cloud property retrieval algorithms [*Menzel et al*., 2008; *Wang et al*., 2011; *Baum et al*., 2012], and the calibration.

King et al. [2003] described the details of the MODIS aerosol and cloud properties in the first version available to the community (collection 4, henceforth C4). *Meyer et al*. [2007] used the MODIS C4 level-3 gridded cloud products to analyze the spatial and temporal trends of tropical ice clouds. With use of both Aqua and Terra MODIS C4 data, *Hong et al*. [2007] studied the climatology of high cloud properties in the tropics. *Zhang et al*. [2010] studied the relationship between surface meteorology and Terra MODIS C4 retrieved liquid water cloud properties in boundary layer cloud regimes. MODIS C4 liquid water cloud properties were also investigated in a number of studies focused on aerosol-cloud interactions [e.g., *Kaufman et al*., 2005; *Lebsock et al*., 2008].

In its time, the MODIS C51 products provided another major change, employing a number of improvements over that in C4 [*Menzel et al*., 2008]. *King et al*. [2013] provided a complete summary of the global cloud property climatology based on Aqua and Terra MODIS level-3 C51 products. Significant changes in the cloud properties were found from collection 4 to collection 5 [*Yang et al*., 2007; *Hong et al*., 2007]. Specifically, greater ice cloud fraction, larger ice cloud optical thickness, and smaller ice cloud effective particle radius were found in C51 compared to C4. Such differences in cloud properties are critically dependent on the surface type (i.e., land or sea). In addition, changes in the cloud optical properties could induce large impacts on the global cloud radiative effects [*Yi et al*., 2013; *Yang et al*., 2015]. For example, cloud particle effective size and optical thickness directly determine the amounts of shortwave and longwave radiation scattered or absorbed by clouds. Cloud top height and cloud temperature also significantly modulate cloud radiative processes. *Yang et al*. [2007] show that the differences in ice cloud properties between MODIS C4 and C5 could induce total cloud radiative forcing differences ranging from -60 W m^{-2} to 20 W m^{-2}, indicating that changes in satellite retrieval of cloud properties could induce huge differences in the estimations of cloud radiative impacts. Thus, it is quite necessary to quantify the differences in different collections of MODIS cloud products to better understand the various impacts of clouds on climate.

However, almost all available comparisons of MODIS data collections are based on the operational level-3 products. The MODIS operational level-3 cloud products aggregate the level-2 retrievals spatially within each 1° equal-angle grid and temporally within each day. We note that in the MODIS daily level-3 aggregation, data from multiple overpasses are saved with respect to individual grid cells. This raises an issue at higher latitudes because cloud properties change quickly and viewing angles also change between overpasses over the same grid cell. Use of an averaged solar zenith angle for a grid cell may not result in the same shortwave flux as that computed from an individual overpass. Monthly aggregations are based on the daily products [*Platnick et al*., 2015]. The gridded products have a much lower volume but lose information provided at the pixel level. There is no way to determine whether the same/consistent numbers of pixels are compared between different collections of level-3 products, which likely induces unknown uncertainties and makes interpretation of differences more difficult. To understand the differences in cloud products between two collections, it makes more sense to begin with the level-2 (instantaneous) products and perform a pixel-to-pixel analysis. The intent of this study is to carry out a systematic analysis comparing the pixel-to-pixel changes between C6 and C51 and to quantify the resulting radiative effects.

The remaining parts of this paper introduce the data and methodology in section 2. Section 3 shows the major results from the comparison. A discussion of C6–C51 cloud radiative effect difference is given in section 4. Summary and concluding remarks are given in sections 5 and 6.

2. Data and Methodology

The Aqua MODIS C51 and C6 level-2 cloud retrieval products (“MYD06_L2”) for 2012 are employed in this study. The cloud products contain variables with 1 km resolution, such as the cloud effective radius (CER), cloud optical thickness (COT), and cloud water path (CWP) [*Platnick et al*., 2003], as well as variables with 5 km resolution, such as the cloud fraction (CF) [*Ackerman et al*., 1998; *Frey et al*., 2008; *Ackerman et al*., 2008], cloud top pressure (CTP), and cloud top temperature (CTT) [*Menzel et al*., 2008] at the pixel level for each 5 min granule (288 granules per day). Ice and liquid water clouds are separated by the MODIS cloud phase product ("Cloud_Phase_Optical_Properties" for the 1 km resolution variables (i.e., CER, COT, and CWP) and "Cloud_Phase_Infrared" from 8.5 μm and 11 μm bands for the 5 km resolution variables (i.e., CTP and CTT) [*King et al*., 2010]. Note that the two cloud phase infrared products may not always agree with each other, as one is based on a pixel-level radiance and the other is based on the mean of the radiances in the 5 km pixel array. In C6 the Cloud_Phase_Optical_Properties algorithm was substantially improved, and this led to different phase determinations for some of the cloudy pixels than in the previous C5 algorithm [*Marchant et al*., 2016; *Platnick et al*., 2017]. The CER, COT, and CWP are the two-channel retrievals using band 7 (2.1 μm) and band 1 (0.65 μm), 2 (0.86 μm), or 5 (1.24 μm). The exact variables are labeled "Cloud_Effective_Radius," "Cloud_Optical_Thickness," and "Cloud_Water_Path" in both C51 and C6.

In this study, the 5 min granules are aggregated to gridded daily, monthly, seasonal, and annual averages similar to operational level-3 products but with higher horizontal resolution of 0.5° × 0.5° in latitude and longitude. The gridding process follows *Smith et al.* [2013] and involves filtering and aggregating data spatially into equal-angle grid boxes and temporally into daily/monthly/yearly results. However, some additional criteria are used in this study to better illustrate the product differences. Note that the level-3 products created for this study are different from the operational MODIS level-3 products.

Due to various changes implemented in the cloud product retrieval process from MODIS C51 to C6, the retrieved cloud products are expected to have disagreements between the two collections. In this study, the products are filtered with the "valid retrieval" flag. The term valid retrieval means that the variable has useful information (variable usefulness flag = 1), a very good confidence level (confidence flag = 3), a retrieval uncertainty lower than 80%, and a nonfill value for the retrieved variable. Pixels are used that are "overcast cloudy" (clear sky restoral flag = 0) and are "near-nadir" observations (with sensor zenith angle smaller than 32°). Note that retrieval uncertainties are not provided for the CTP and CTT with 5 km resolution. The determination of what comprises a valid cloud retrieval may change between collections; the decision to use such a flag is left to the product user. The level-3 cloud fraction is derived similarly to the operational level-3 cloud optical properties cloud fraction (i.e., "Cloud_Retrieval_Fraction_Combined"), as it is based on the daytime-only Cloud_Phase_Optical_Properties retrieval instead of the cloud mask to distinguish different cloud fractions in liquid water and ice phases.

Pixels with valid retrievals within a calendar day are first aggregated and gridded to a daily average. At higher latitudes, results from only one overpass are used for each grid cell in a daily average; the overpass is chosen that has the lowest grid cell mean sensor zenith angle. The corresponding monthly, seasonal, and annual averages are generated from the daily averages. The grid box values (i.e., CER, COT, CWP, and CTP) are weighted by the respective ice/liquid water cloud pixel counts for the spatial (i.e., global) and temporal (i.e., monthly and yearly) aggregation and averaging processes. Here we consider two cases as the basis for comparison: (1) only the pixels where both C51 and C6 have valid retrievals and identical cloud phase are aggregated and (2) all pixels are aggregated for which C51 and C6 have valid retrievals and identical cloud phase. A special note is that the 5 min granules that exist only in C51 or in C6 (such cases exist but are very rare) are still omitted in case 2.

3. Results

The results shown below are based on the annual averages of case 1 unless otherwise noted. Ice clouds and liquid water clouds are discussed separately. The case 2 results are discussed at the end of this section with emphasis on the largest differences from case 1. Table 1 shows a summary of the global averaged cloud optical and physical properties for both case 1 and case 2. Ice clouds generally display greater C6–C51 differences in the microphysical and optical properties such as CER and COT, while liquid water cloud differences are mostly in CWP, CTP, and CTT. Overall, cases 1 and 2 show similar product differences for ice cloud properties but have larger differences for liquid water cloud properties. For some variables, the liquid water cloud differences between collections for case 2 are more than twice the case 1 collection differences (i.e., CWP and CTP).

Table 1. Summary of the Global Averaged Cloud Properties in Case 1 and Case 2[a]

	Ice Cloud			Liquid Water Cloud		
	C51	C6	C6–C51	C51	C6	C6–C51
CER	24.94	31.63	6.69	12.64	12.35	−0.29
	(23.91)	(31.17)	(7.26)	(12.68)	(14.64)	(1.96)
COT	16.20	12.70	−3.50	13.69	14.26	0.57
	(15.81)	(12.47)	(−3.34)	(13.20)	(14.44)	(1.24)
CWP	242.43	234.10	−8.33	109.89	111.00	1.11
	(239.90)	(237.84)	(−2.06)	(106.31)	(136.92)	(30.58)
CTP	294.17	284.54	−9.63	816.70	811.37	−5.33
	(297.02)	(287.20)	(−9.82)	(838.42)	(813.74)	(−24.68)
CTT	228.44	227.09	−1.35	279.63	277.77	−1.86
	(228.59)	(227.40)	(−1.19)	(280.75)	(277.96)	(−2.79)
CF	0.186	0.166	−0.020	0.179	0.211	0.032
	(0.200)	(0.182)	(−0.018)	(0.192)	(0.228)	(0.036)

[a]Values shown in parentheses are from case 2. CER is in the unit of microns, and CWP is in the unit of g m^{-2}. CTP and CTT are in the units of hectopascal and kelvin, respectively.

3.1. Ice Cloud Physical and Optical Properties

Figure 1 shows the histograms of ice CER, COT, CWP, CTP, CTT, and CF occurrence frequencies. It is notable that the peak of the CER frequency shifts from about 23 μm in C51 to about 32 μm in C6 (more than 25% difference). Higher-latitude regions (>60°N or >60°S) have even larger relative CER differences of more than 35% (Figure 2d). The significant differences in CER between C51 and C6 can be attributed in part to the

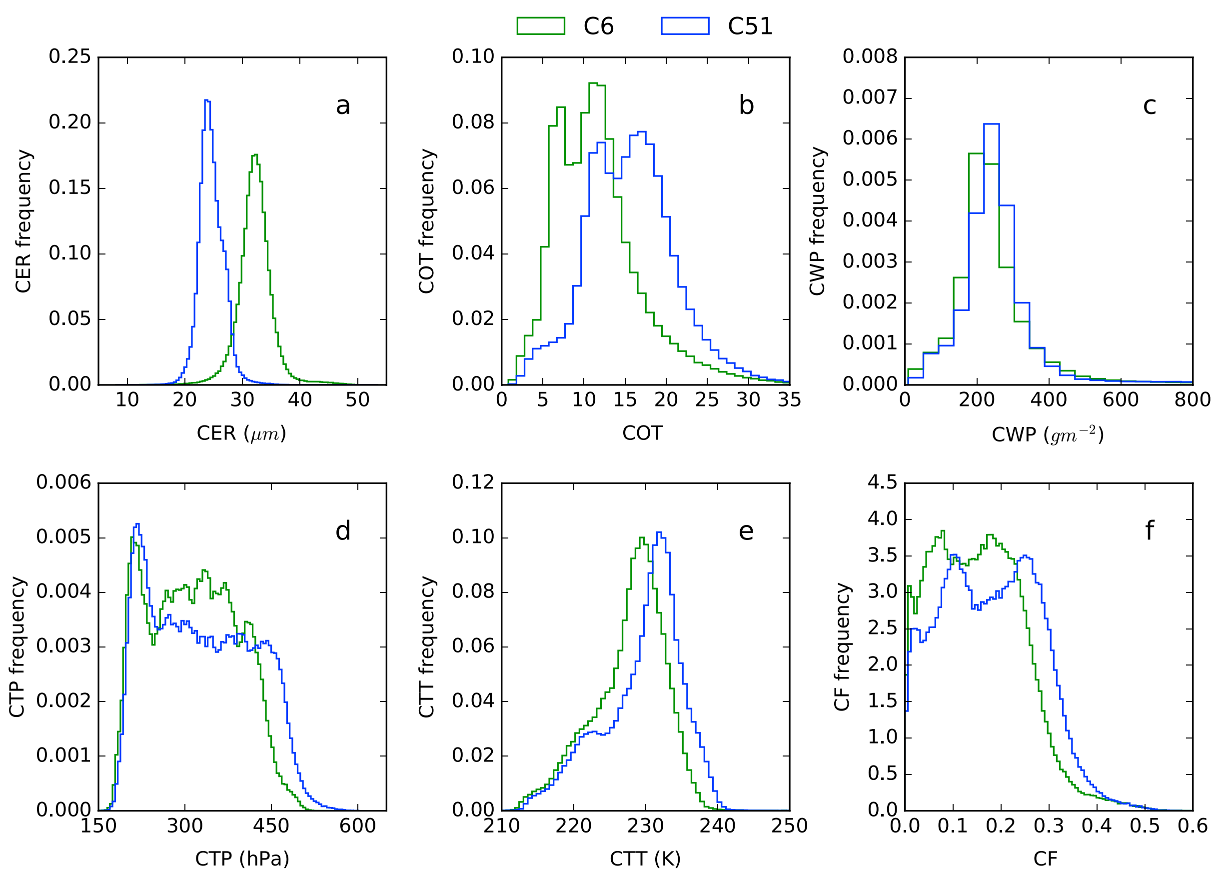

Figure 1. The occurrence frequencies of annual averaged ice cloud properties: (a) cloud effective radius (CER, unit: μm), (b) cloud optical thickness (COT), (c) cloud water path (CWP, unit: g m^{-2}), (d) cloud top pressure (CTP, unit: hPa), (e) cloud top temperature (CTT, unit: K), and (f) cloud fraction (CF).

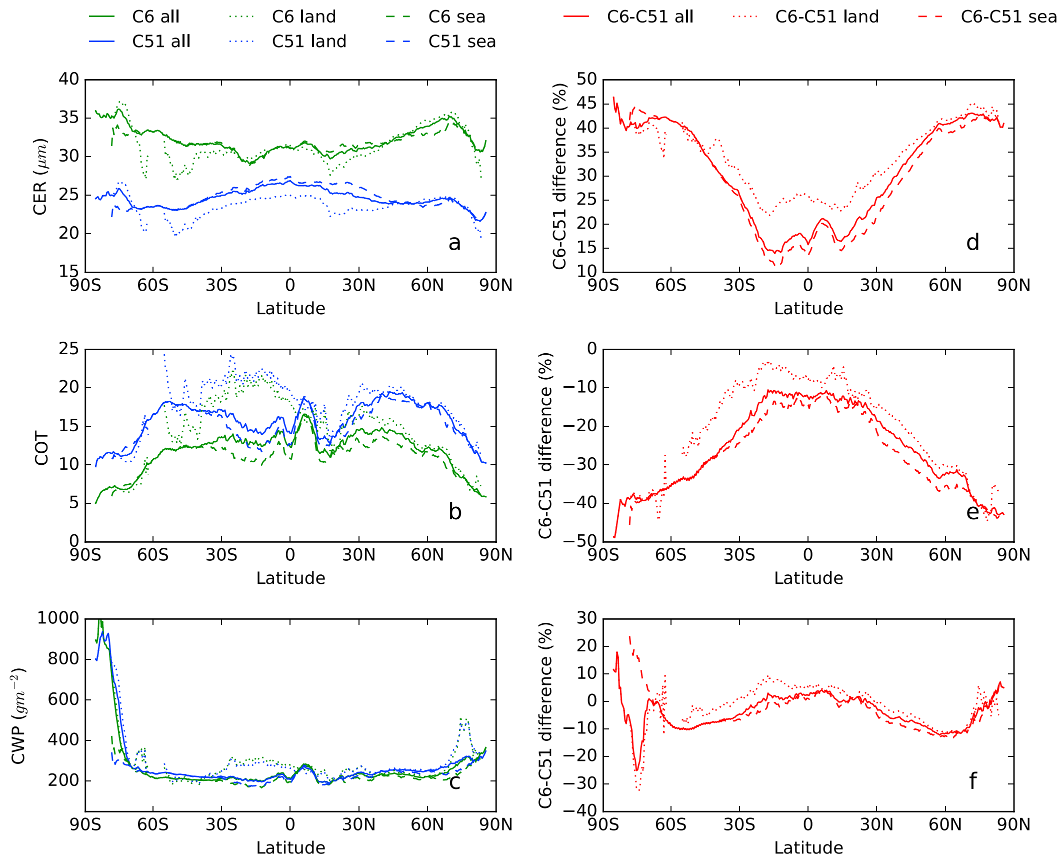

Figure 2. Zonal mean annual averaged ice cloud optical properties: (a) CER, (b) COT, and (c) CWP in collection 6 data set and (d–f) the corresponding differences between MODIS collection 6 and collection 5.1.

change of ice cloud particle scattering model in the MODIS ice cloud retrieval process. In C51, the ice model consists of a mixture of habits with smooth surfaces [*Baum et al.*, 2005], while in C6 the ice model consists solely of a severely roughened aggregate of solid columns [*Platnick et al.*, 2017]. The histogram of COT shows that the C51 values tend to peak around 12 and 17, while the C6 COT has increased bimodal peaks around 6 and 12. The histograms of C6 and C51 CWP are quite similar, even with differences in the inferred COT and CER between the two collections.

A number of improvements were made in C6 to improve the inference of cloud top pressure and temperature and cloud thermodynamic phase (note that this is Cloud_Phase_Infrared rather than Cloud_Phase_Optical_Properties) as noted in *Baum et al.* [2012]. One of the most important changes was the implementation of slight modifications to some of the spectral response functions for the 15 μm channels that affected the CO_2 slicing technique. This did not impact the MODIS measurements but rather the radiative transfer model used to simulate the measurements. This change in the response functions resulted in the ability to provide CTP and CTT at 1 km resolution. In addition, the C6 IR-based cloud thermodynamic phase has an increased sensitivity to thin cirrus. The approach uses cloud emissivity ratios for different IR channel pairs to improve the cloud phase sensitivity of optically thin ice clouds [*Baum et al.*, 2012; *Heidinger and Pavolonis*, 2009; *Pavolonis*, 2010]. But in this study, the 5 km CTP and CTT are analyzed since C51 only has the 5 km cloud top properties.

As shown in Figure 1, the CTP histogram indicates a narrower distribution for C6, with more frequent C6 ice cloud at lower CTP values between 280 and 420 hPa (i.e., increase in cloud heights) than in C51. The ice CTT peak frequency slightly decreases from C51 to C6, and the ice CF peaks shift to lower values.

The retrieved zonal mean and global distributions of ice CER in C6 and the C6–C51 differences are shown in Figures 2a, 2d, 3a, and 3d, respectively. CER increases in the global average by 6.68 μm as shown in Table 1.

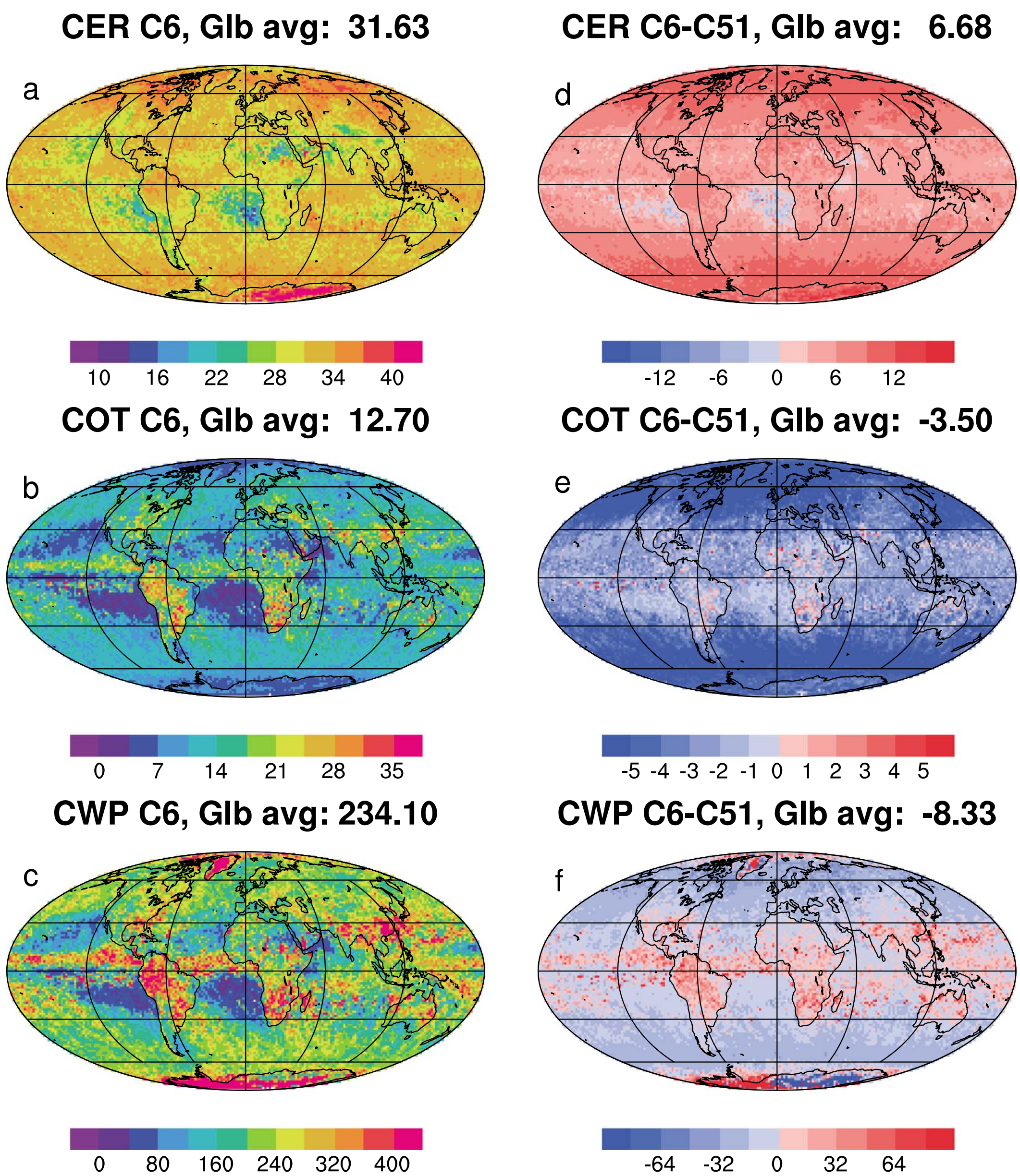

Figure 3. Global annual averaged distributions of ice cloud optical properties: (a) CER (unit: μm), (b) COT, and (c) CWP (unit: g m^{-2}) in collection 6 data set and (d–f) the corresponding differences between MODIS collection 6 and collection 5.1.

From Figure 2a, it is interesting to note that the CER tends to decrease with latitude in C51, while the CER tends to increase with latitude in C6. It is still a matter of conjecture why ice clouds at the higher latitudes tend to have larger effective sizes in C6. The differences could be due to the changes in cloud optical properties from the new ice cloud models and lookup tables or an artifact of changes to the surface characteristics (e.g., temperature and albedo) in C6. *Platnick et al.* [2017] find that the increase of cloud single-scattering albedo from C51 to C6 at the 2.1 μm channel induces larger retrieved ice CER. However, with the decrease in the asymmetry parameter from the severely roughened model in C6 in comparison with the smooth ice habits adopted in C51, the inferred COT decreases for the same reflectance [*Baum et al.*, 2014]. If the CWP remains constant, this implies the potential for an increase in the CER in C6. The ice particle model has been found to be critically important for the ice cloud property retrievals [*Zhang et al.*, 2009] and radiative transfer simulations involving ice clouds [*Yi et al.*, 2016]. Only ice clouds within the

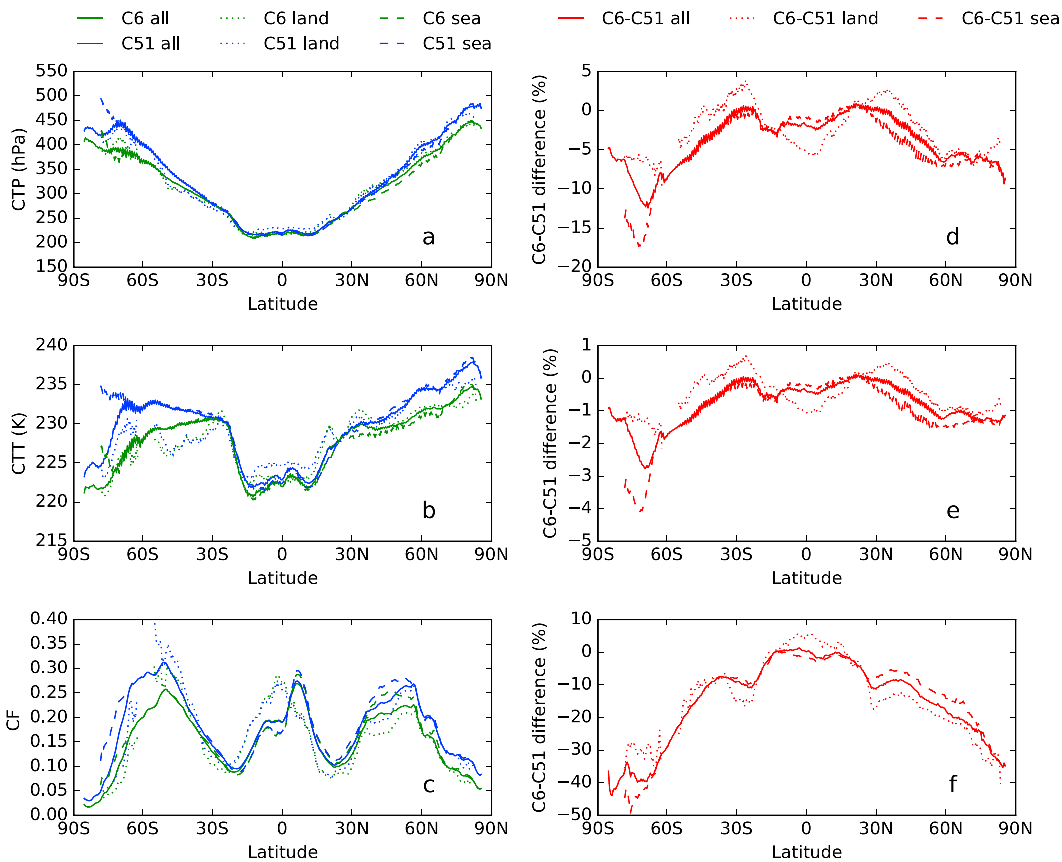

Figure 4. Zonal mean annual averaged ice cloud top properties: (a) CTP, (b) CTT, and (c) CF in collection 6 data set and (d–f) the corresponding differences between MODIS collection 6 and collection 5.1.

tropical region have CER values larger than about 25 μm in C51, whereas very few areas have CER lower than 25 μm (including west coasts of North America, South America, Africa, and South Asia) in C6. These are all areas where aerosols are abundant and the aerosol impacts are prominent. *Jiang et al.* [2011] have pointed out that CER of ice clouds from satellite observations decreases with aerosol optical thickness over the aforementioned regions. The C6–C51 difference in CER is almost globally positive, except in regions of persistent marine stratocumulus where there is a low frequency of ice cloud. Better agreement is found in the tropics, while the C6–C51 CER difference grows with the increase of latitude. Near the South Pole, the differences can be up to 15 μm. The results in Figure 2d indicate that over the tropical and subtropical areas, CER differences are larger over land than over ocean.

The ice COT in C51 and C6 (Figures 2b, 2e, 3b, and 3e) indicates better agreement than the CER comparison, although the differences also increase with the latitude. The C51 COT is globally larger than the C6 COT by about 25%, which is consistent with the use of the ice habit model with smooth surfaces in C51. The C6–C51 largest COT differences peak near the storm track regions in the Northern and Southern Hemispheres where differences are about −5. COT differences over ocean are generally larger than those over land except for Antarctica and Greenland.

The C51 and C6 ice CWP show generally good agreement globally and regionally, especially for the regions between 30°N and 30°S (Figures 2f, 3c, and 3f). This is interesting because even with the rather major change in the ice model bulk scattering properties from C51 to C6 that results in COT decreasing and CER increasing, the CWP does not change very much. The histograms (Figure 1c) of C51 and C6 CWP show that their peaks overlap near 200 g m^{-2}. Larger CWP differences exist in the southern oceans and near the South Pole, but the zonal mean differences are generally below 20%. However, the land and sea curves in Figure 2f and the spatial distribution in Figure 3f show that there are clearly some

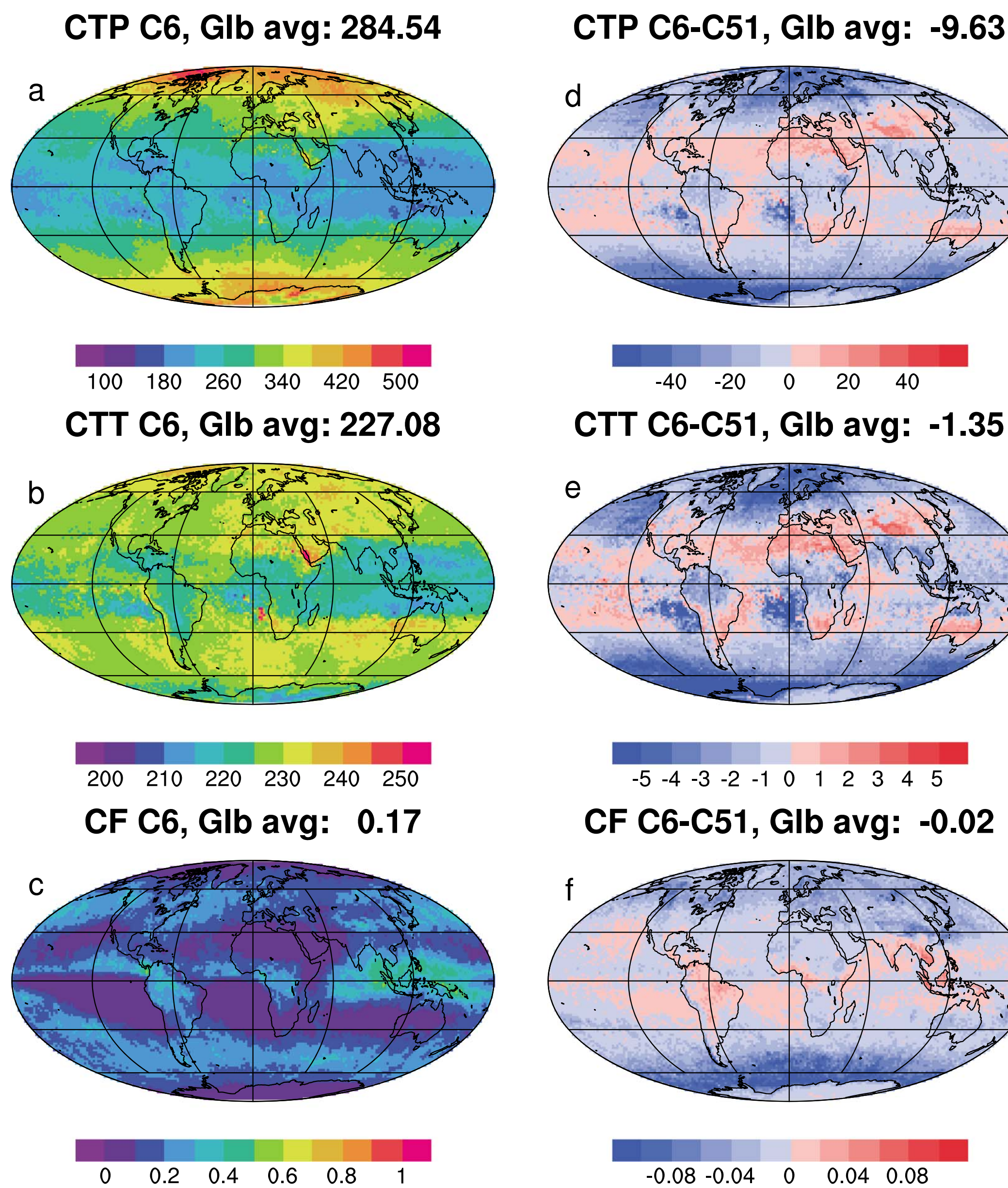

Figure 5. Global annual averaged distributions of ice cloud top properties: (a) CTP (unit: hPa), (b) CTT (unit: K), and (c) CF in collection 6 data set and (d–f) the corresponding differences between MODIS collection 6 and collection 5.1.

compensating biases between the land and ocean areas that result in small zonal mean differences, especially in the Southern Hemisphere between 0 and 45°S. Additionally, the tropical land areas show somewhat larger CWP C6–C51 differences than over ocean.

The ice CTP generally ranges from 220 hPa to 500 hPa and is lowest over the tropical areas, especially over western Pacific Ocean and Southeast Asia. The C51 and C6 CTP have small differences (within 10% regionally) with a global average around 284 hPa (Figures 4a, 4d, 5a, and 5d). As noted previously, the comparisons here are made with the 5 km products only in C51 and C6. The most significant CTP differences (negative) are found around 60°N and 60°S. We find that the CTT corresponds well with the CTP, having the lowest CTT over the region where CTP is lowest. The C6–C51 difference in CTT is much less apparent than that with CTP. Interestingly, the subsidence regions around ±30° have positive differences for CTP and CTT over land, while the global averaged difference is negative, although it should be noted that ice cloud occurrences in these

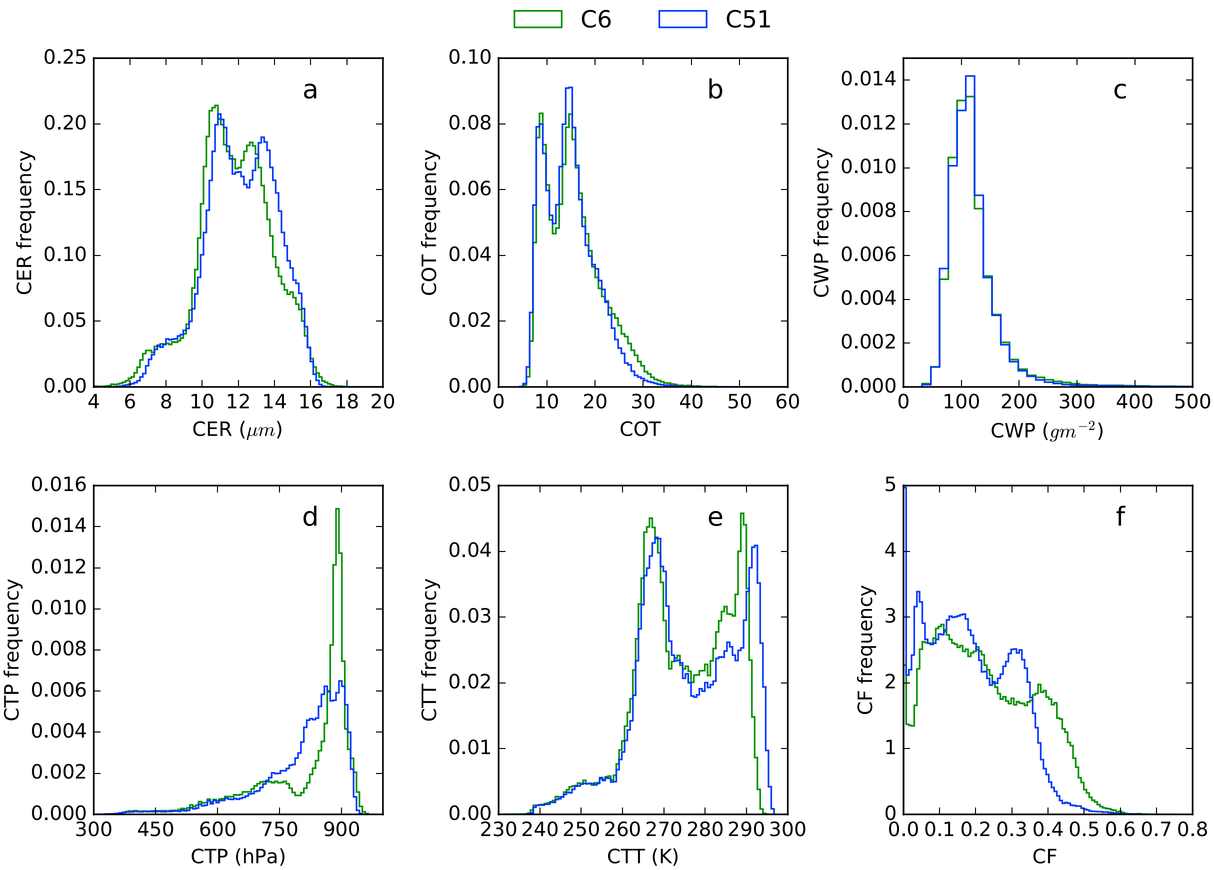

Figure 6. The occurrence frequencies of annual averaged liquid water cloud properties: (a) CER, (b) COT, (c) CWP, (d) CTP, (e) CTT, and (f) CF.

regions are low. The ice CF is largest near the equator and at the midlatitude around 50°N and 50°S, with CF as high as 0.3 in C6. The ice CF C6–C51 difference, however, is within 10% from 40°N to 40°S. At higher latitudes (70°N and 70°S), regional differences can be as large as 40%. Positive C6–C51 CF differences are mostly restricted to the land areas over the tropics (Figure 5f).

While the ice cloud physical properties do not show large C6–C51 difference from the global average perspective, considerable differences are evident regionally, such as the positive CTT difference over subtropical land areas. The CTT is also lower in C6 to the west of South America and Africa, although ice clouds are less common in these subsidence regimes dominated by stratocumulus (see Figure 5e).

3.2. Liquid Water Cloud Physical and Optical Properties

The histograms in Figure 6 show the occurrence frequencies of liquid water CER, COT, CWP, CTP, CTT, and CF. C51 and C6 mostly have very similar distributions, but there are some shifts in the peaks. For example, the liquid water CER and CTT peaks in C6 slightly shift toward lower values. The histogram clearly shows a shift to smaller values from the two-peak CER frequency mode in C51 to the two-peak mode in C6. Liquid water CTP frequency, however, shows a decrease around 700–800 hPa and an increase around 880 hPa. In comparisons of MODIS C51 to CALIOP, one of the major biases in CTP was found in maritime stratocumulus regions [*Holz et al.*, 2008, 2016]. In C6 this bias was mitigated by adopting a refined IR window method that uses monthly mean latitudinally dependent “apparent IR lapse rates” to determine low-level liquid water cloud height over ocean [*Baum et al.*, 2012]. Liquid water CF peaks shift to higher values in C6 meaning that more liquid water clouds are analyzed successfully.

The liquid water CERs in C6 and C51 consistently decrease with increasing latitude from the equator to the poles (Figures 7a and 8a) with the CERs over ocean significantly larger than those over land. The relative difference between C51 and C6 is close to zero near the equator and is the largest near the South Pole (~10%).

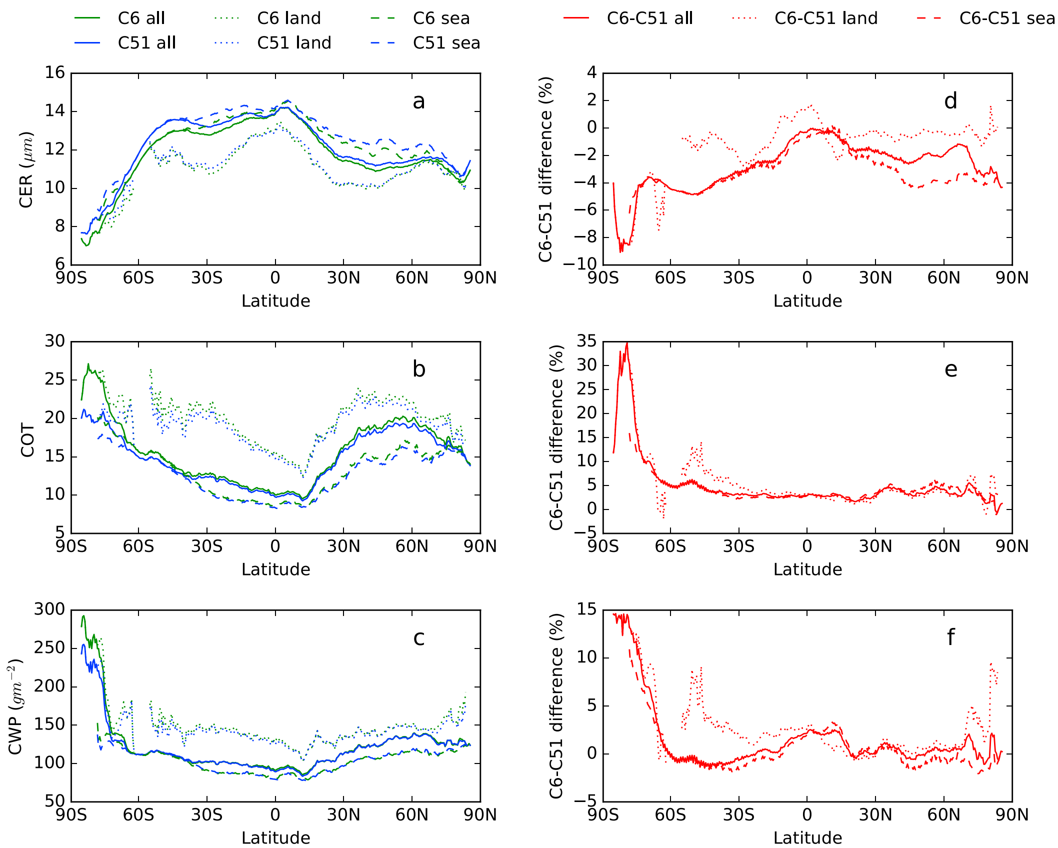

Figure 7. Similar to Figure 2 but for liquid water cloud properties.

From the globally averaged perspective, the two collections have similar liquid water CERs of about 12 μm. The largest regional difference of liquid water CER is noticeable over the tropical warm pool region (up to 4 μm). Although little difference in liquid water CER is observed for global and zonal averages, regional CER differences over the tropical and subtropical oceans may be as large as 3 μm. These regional differences appear to be related to cloud morphology differences, with smaller CER in C6 for regions corresponding to mostly closed-cell stratocumulus clouds and larger C6 CER in areas dominated by shallow cumulus [e.g., *Wood et al.*, 2008]. Since case 1 does not include any partly cloudy pixels and only cases where both collections identify liquid water clouds, this rules out changes in the cloud mask or phase identification as the main driver and suggests that changes in the radiative transfer and lookup tables used for the various collections of MODIS cloud optical property retrievals drive these differences.

For the liquid water COT (Figures 7b and 8b), C6 is globally larger than C51. Not only does the COT increase from lower to higher latitudes, but the C6–C51 relative differences of COT also follow similar variations. Over the higher-latitude region of the Southern Hemisphere (>60°S), the relative COT differences can reach about 35% (Figure 8e).

Again, C6 liquid water CWP is higher than the C51 counterpart globally (Figures 7c and 8c). Except for certain regions near the equator (i.e., western Pacific and Amazonia) and the higher latitudes in the Southern Hemisphere, the C6 and C51 CWP agree well. For the Northern Hemisphere, the C6–C51 CWP difference is more evident over ocean than over land.

Overall, the liquid water clouds over land and tropical oceans have consistent changes from C51 to C6 in that the CTP and CTT both decrease, indicating that the liquid water clouds have higher and colder cloud tops in C6 (Figures 9 and 10) outside of marine stratocumulus regions. For the areas dominated by marine stratocumulus, e.g., the eastern North Pacific and eastern North Atlantic near 30°N, the eastern South

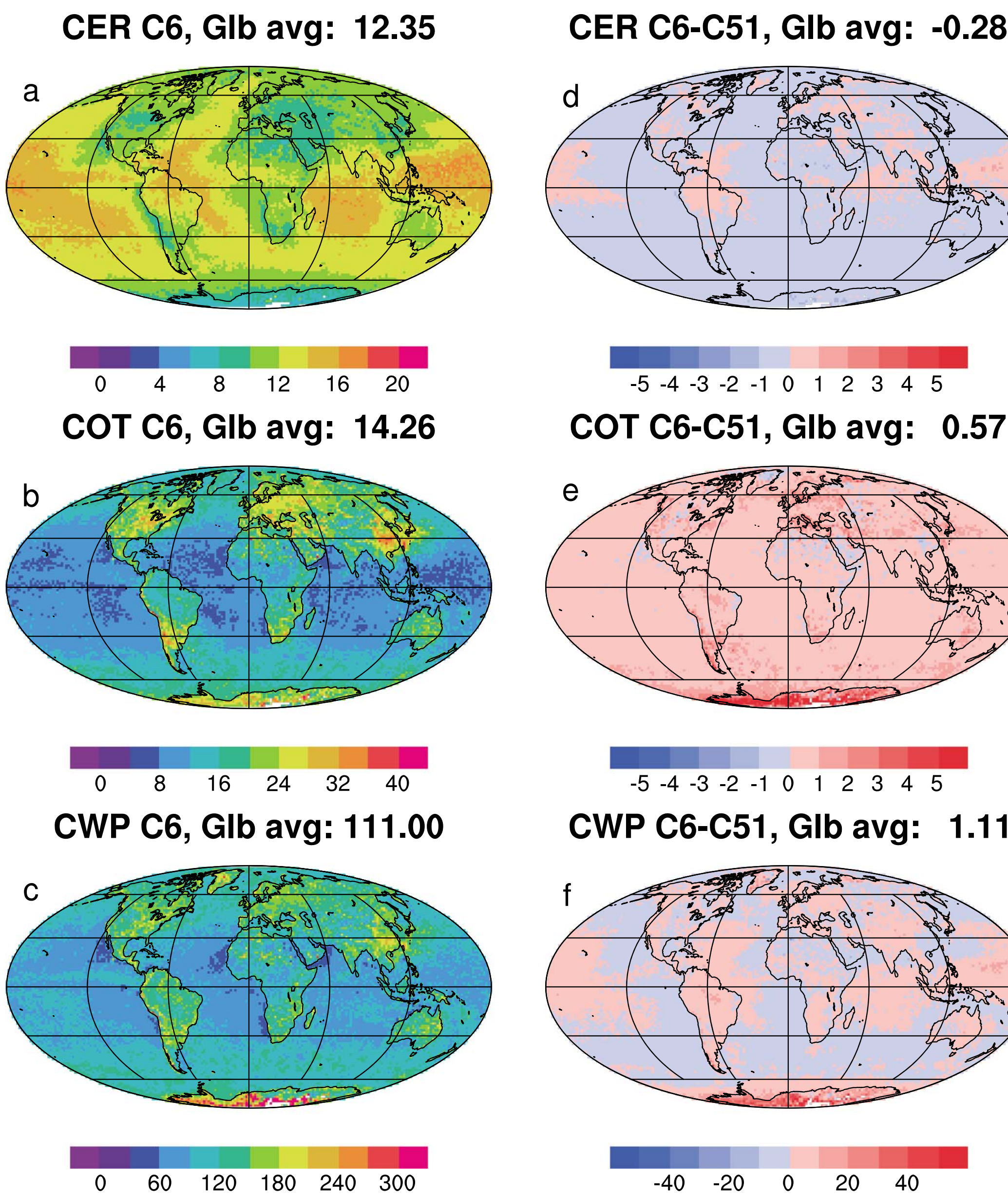

Figure 8. Similar to Figure 3 but for liquid water cloud properties.

Pacific and eastern South Atlantic near 27°S, as well as the southern oceans below 30°S, the liquid water clouds have larger CTP with near-zero changes or slight decreases in CTT. In contrast, there are small corresponding CTT changes found in relation to these CTP changes, which is expected since the maritime stratocumulus regions tend to have temperature inversions. The globally averaged liquid water CF is about 0.21. Mostly, the liquid water CF has negligible C6–C51 differences except for the higher-latitude regions in both hemispheres (especially for the southern oceans) where the relative CF difference is large but the absolute difference is small.

3.3. The Representativeness of the Results: Comparisons Between Case 1 and Case 2

Because the above results are based on the subset of pixels when both C51 and C6 have valid retrievals, we now test how well these results represent the entire data set. Further comparisons are made between case 1, when both C51 and C6 have valid retrievals, and case 2, when C51 and C6 individually have valid retrievals. In the following analysis, only the results that are significantly different from case 1 will be presented.

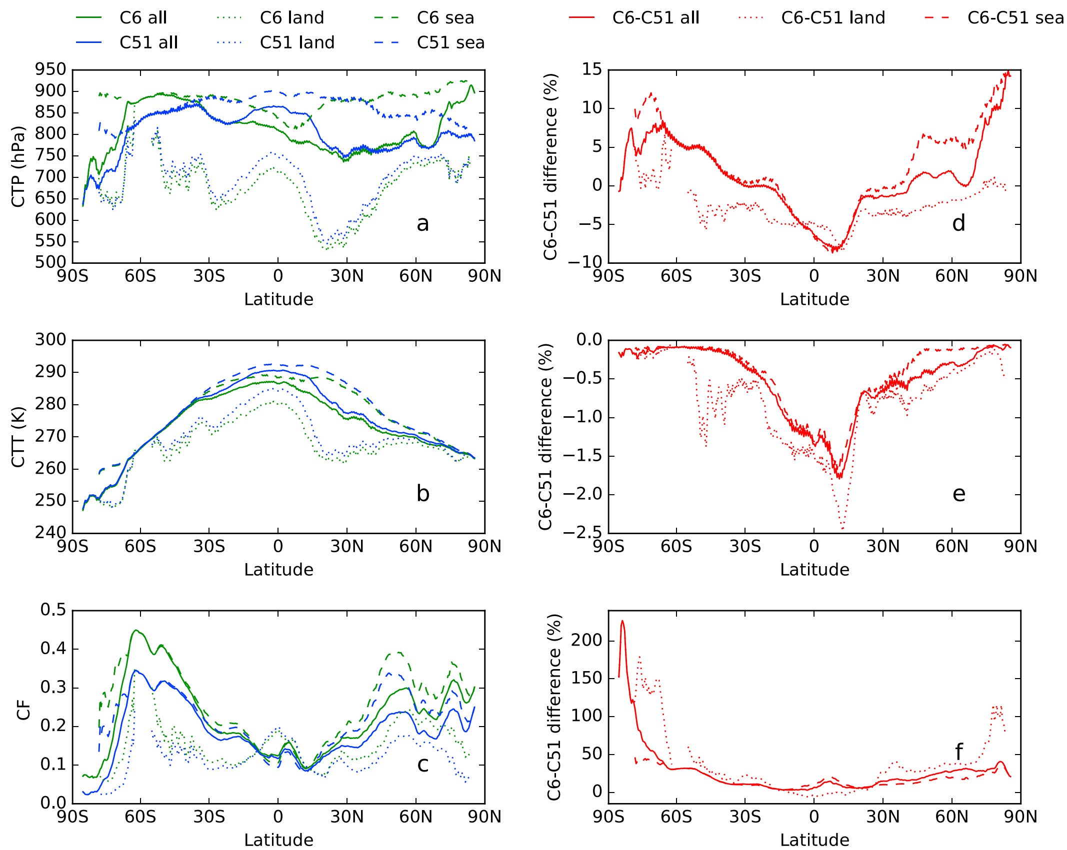

Figure 9. Similar to Figure 4 but for liquid water cloud properties.

3.3.1. Ice Clouds

Both C51 and C6 ice CERs in case 2 have similar globally averaged values with those of case 1, except that the C6–C51 CER difference is slightly larger in case 2 (Table 1). The globally averaged COT are consistent in general for both cases but slightly more negative C6–C51 differences are found in the tropical region in case 2 (figure not shown). The globally averaged CWP values for C51 and C6 are closer when all valid pixels are considered in case 2. Although the regional C6–C51 differences in CWP increase in case 2, the impact of compensating biases actually reduces the globally averaged value. The zonally averaged plots indicate that there are larger differences in the higher latitudes, especially in the Southern Hemisphere. This is likely due to the increased cloud phase disagreement between C6 and C51 in these regions [*Marchant et al.*, 2016]. However, both cases display the same variation with latitude (figures not shown).

For the ice cloud physical properties including cloud top pressure, cloud top temperature, and cloud fraction, the results from case 1 and case 2 match closely.

3.3.2. Liquid Water Clouds

The liquid water CERs agree well in C6 and C51 in case 1, although there are some differences in the spatial distribution patterns with the maximum difference in CER lower than 4 μm. However, in case 2, the CER in C6 is significantly larger by about 2 μm globally (Figure 11c). The increase in liquid water cloud effective particle size is especially apparent over the tropical ocean. The maximum C6–C51 difference in CER for case 2 can be larger than 5 μm regionally, which increases by more than 15% for the zonal averaged CER (figure not shown).

The liquid water COTs are similar for both cases 1 and 2, with the global average C6–C51 difference near 1.24. A slight decrease of COT in C6 in case 2 is found over the tropical and Southern Hemisphere oceans (figure not shown).

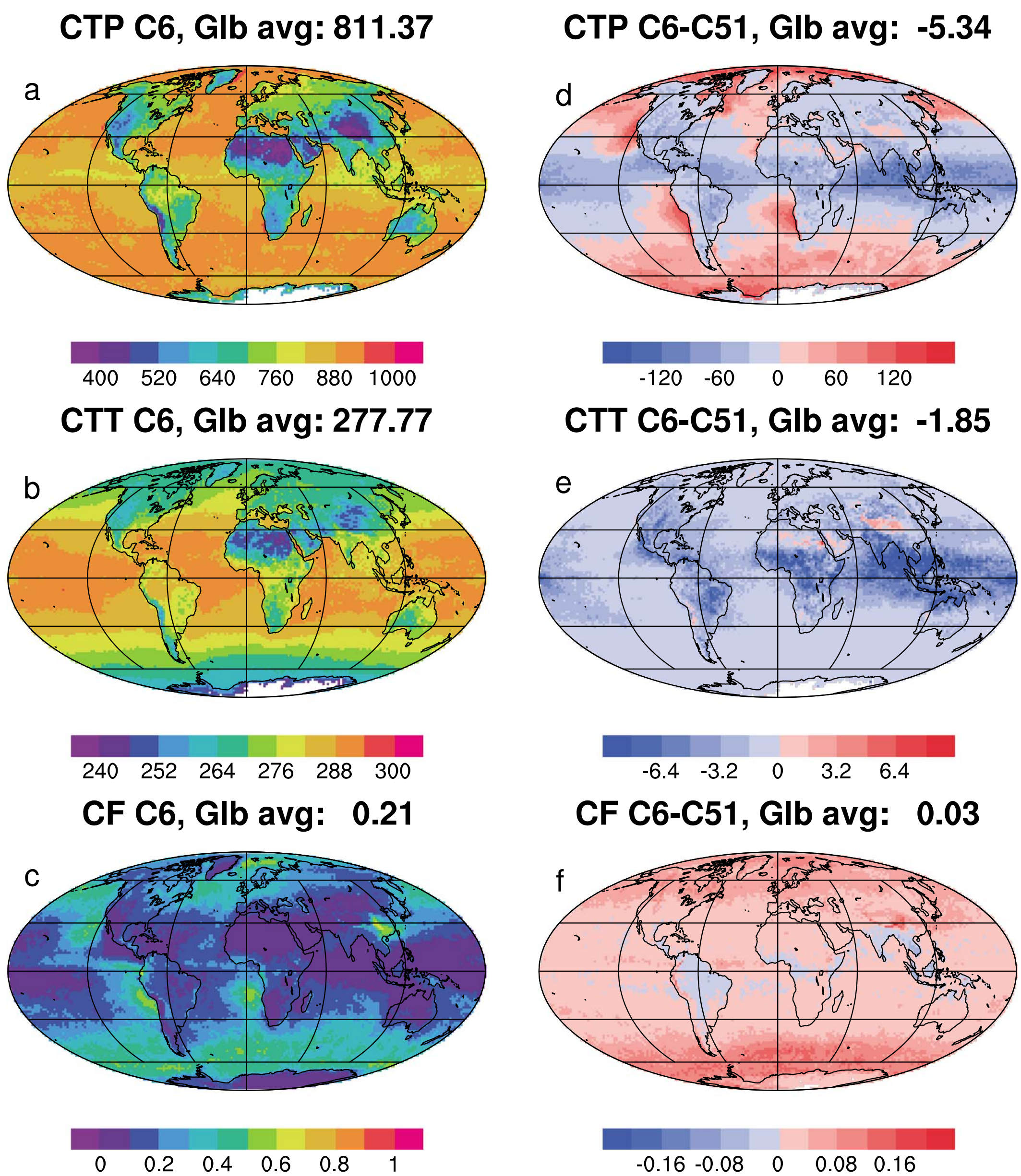

Figure 10. Similar to Figure 5 but for liquid water cloud properties.

The liquid water CWP is much larger for C6 in case 2 and yields a remarkably higher C6–C51 difference (30.58 g m^{-2}) compared with that in case 1 (1.11 g m^{-2}). In addition to the larger C6–C51 difference found over tropical oceans, several high-latitude land regions also have much larger CWP (Figure 11d). This increase in liquid water CWP is expected since CWP is calculated from the (increased) CER.

Interestingly, the liquid water CTP for C51 in case 2 is significantly larger than that of case 1. This leads to a difference of about −25 hPa in globally averaged CTP between C6 and C51 (Figure 12c). Apart from the higher CTP in the marine stratocumulus regions on the west coast of North America, South America, Southern Africa, and the southern oceans, we find lower CTP over land and Southeast Asia. Correspondingly, negative C6–C51 CTT differences are found over land.

3.3.3. Differences in the Number of Cloudy Pixels

How are the differences in the cloud optical property variables between cases 1 and 2 related to the differences in the number of valid pixels in each case? Differences in the number of valid pixels may be

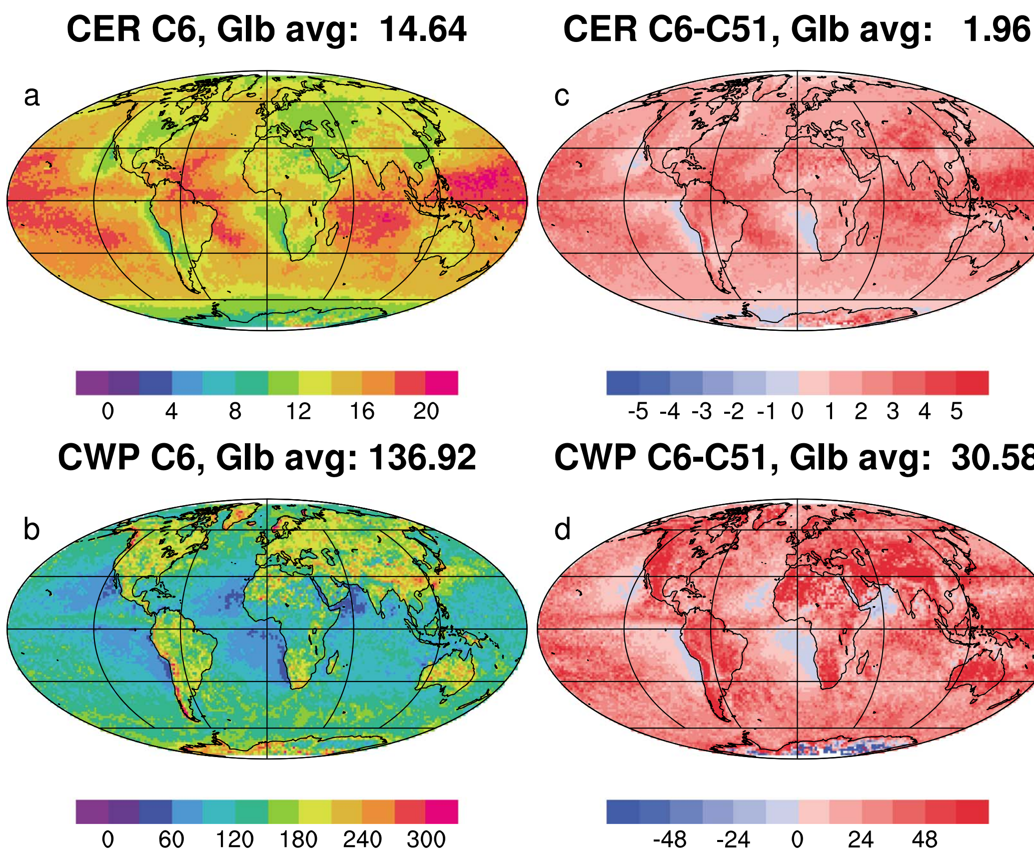

Figure 11. Similar to Figure 8 but for liquid water cloud properties in case 2.

related to a number of changes between the collections, including the cloud mask, thermodynamic phase classification, or the retrieval failure rate. We calculate the relative percentage difference in the number of valid pixels within each grid box, which is defined as the number of valid pixels in case 2 minus that in case 1, then divided by case 1. A summary of the relative pixel difference is provided in Table 2.

For the 1 km resolution ice cloud optical properties (i.e., CER, COT, and CWP), the C51 and C6 in case 2 contain an average of about 30% and 15% more pixels compared with case 1, respectively (Figure 13 and Table 2). The areas with more than 50% more valid pixels include the northern Africa and high-latitude land regions in both hemispheres in C51. In C6, the increase in valid pixels is found primarily over subtropical oceans (i.e., west coast of South America and west coast of South Africa) and also northern Africa. Although there are more ice cloud pixels in case 2, no major differences are found for the optical properties in the comparison of case 1 and case 2. Less than ~5% more pixels are found in case 2 for ice cloud physical properties (i.e., CTP, CTT, and CF), and they have mostly the same features as case 1.

However, the C6–C51 differences of liquid water cloud optical and physical properties are apparently more affected by the number of liquid water cloud pixels. For 1 km resolution optical properties, large differences are found in case 2 of C6 where many more pixels exist (globally about 66% more, see Figure 14c). Particularly in the 30°S–30°N region, most land and ocean areas have more than twice as many pixels. Since case 1 required valid pixels in both collections, this indicates that C6 has more valid retrievals of liquid water clouds than C51. These additional pixels in C6 may be due to several changes, including the thermodynamic phase algorithm and the use of the new 1 km cloud top pressures [*Baum et al.*, 2012; *Platnick et al.*, 2017]. As a result, the C6–C51 differences of CER and CWP are greatly increased, while COT is slightly increased in case 2. Comparatively, only less than 8% additional pixels (mostly over land) are found in case 2 for C51 (Figure 14a). Not surprisingly, little difference is found between case 1 and case 2 for C51 liquid water CER, COT, and CWP. For the 5 km resolution liquid

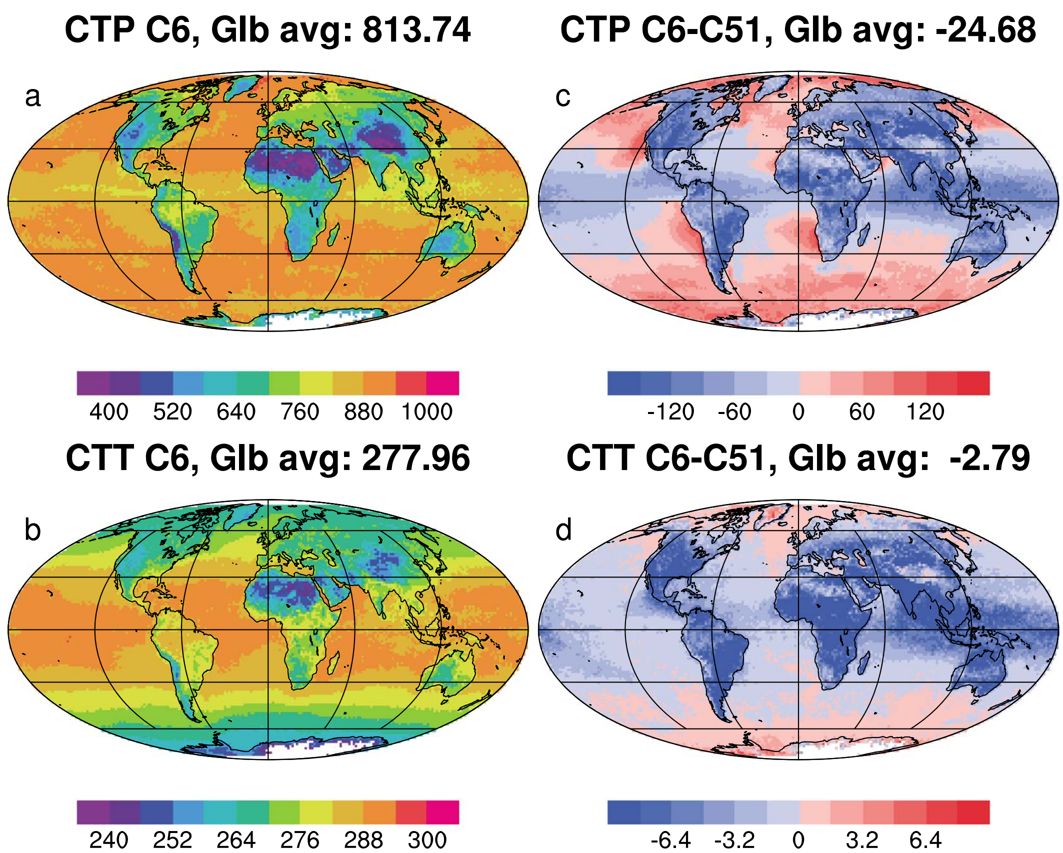

Figure 12. Similar to Figure 10 but for liquid water cloud properties in case 2.

water cloud physical properties, the C51 case 2 has noticeably more pixels (close to 27%, especially over land), while C6 only has 3.6% more.

4. Impact of the C6–C51 Differences on Cloud Radiative Effect

Given the noticeable C6–C51 product differences in cloud properties, what are their impacts on the cloud radiation and the Earth's energy budget? Simulations of the total (only ice and liquid water) cloud radiative effect for case 1 are calculated with the rapid radiative transfer model for GCM (RRTMG) [*Iacono et al.*, 2008]. Ice cloud optical property parameterization schemes specifically made for C51 and C6 are developed and implemented in the RRTMG SW and LW models. The liquid water cloud optical property parameterization is based on *Hu and Stamnes* [1992] (RRTMG built-in option), which is very similar to the liquid water cloud model assumed for MODIS C51 and C6 retrievals. The ERA-Interim reanalysis [*Dee et al.*, 2011] is used to provide atmospheric profile, surface temperature, and surface albedo. Both ice and liquid water clouds are treated as single-layer clouds in the simulation. Random-maximum cloud overlap assumption is used. The

Table 2. Comparison of the Number of Valid Cloudy Pixels in Case 1 and Case 2[a]

	Ice Cloud		Liquid Water Cloud	
	C51	C6	C51	C6
1 km variables	30.61%	15.27%	8.05%	66.11%
5 km variables	4.48%	4.46%	26.79%	3.60%

[a]Values are shown in relative percentage that is defined as case 2 value minus case 1 value and then divided by case 1 value and multiplied by 100.

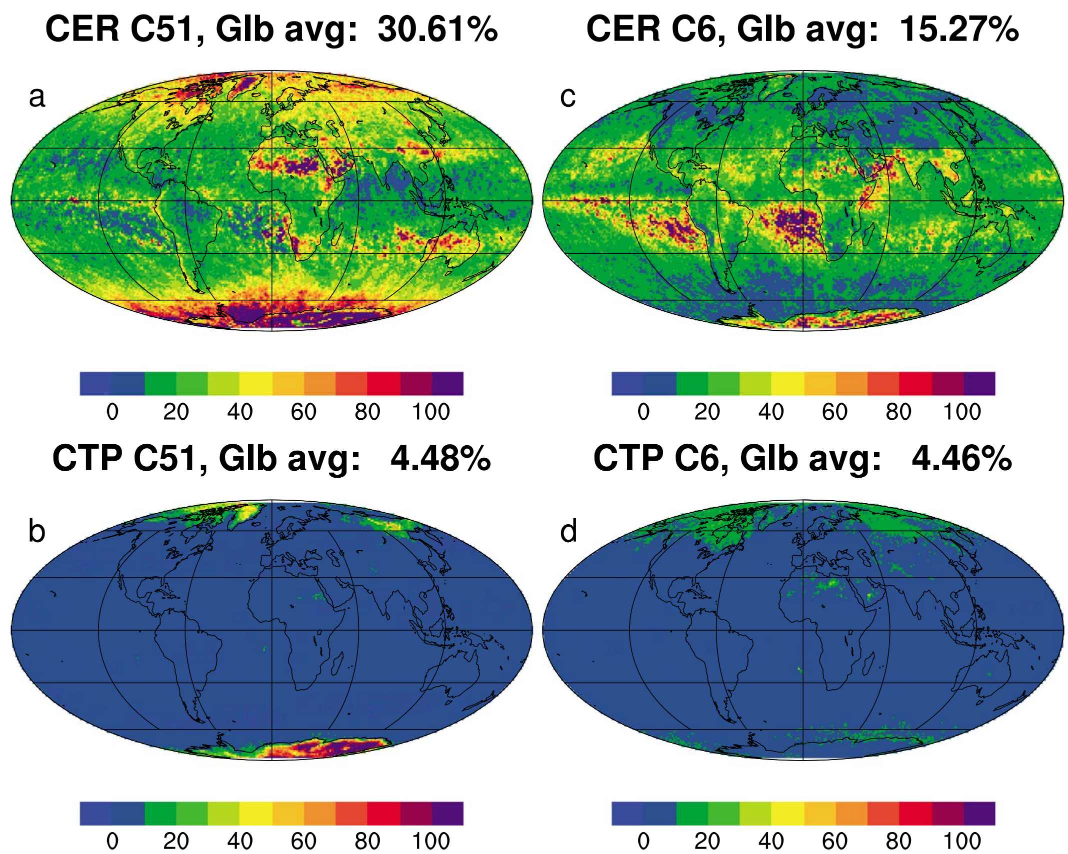

Figure 13. The relative difference between case 1 and case 2 in the number of valid pixels included in the aggregation for ice cloud: (a) CER C51, (b) CTP C51, (c) CER C6, and (d) CTP C6.

cloud radiative effect (CRE) is defined as the net radiative flux difference between all-sky and clear-sky at the top of the atmosphere (TOA).

Figure 15 shows the TOA annual averaged total cloud SW, LW, and net CRE for the C6 and C51. The Clouds and the Earth's Radiant Energy System (CERES) Energy Balanced And Filled (EBAF) cloud radiative effect product is shown as the benchmark for comparison. The corresponding C6–C51 differences, the C6-EBAF differences, and the C5-EBAF differences are shown in Figure 16. CERES EBAF (Figures 15a–15c) shows the global averaged SW, LW, and net CRE to be −46.97, 25.71, and −21.26 W m^{-2}. The C6 CREs (Figures 15d–15f) provide close comparisons with EBAF, with globally averaged SW and LW bias within 4 and 6 W m^{-2}, respectively. However, the C51 CRE simulations have significant overestimation in the SW CRE than the CERES EBAF. Note that there are some discrepancies regionally. Specifically, the C6 SW CRE is overestimated in the midlatitudes in both Northern and Southern Hemispheres (Figure 16d) but is underestimated especially in the tropics. The C6 LW CRE is comparable to the CERES EBAF at the middle and high latitudes but still has a low bias in the tropics (Figure 16e). Although the C6 CRE simulation is comparable to the CERES EBAF observations in the global average, large regional discrepancies still exist (Figure 16f). The CRE differences between C6 and C51 largely stem from the SW spectrum where the SW CRE difference is 17.94 W m^{-2} globally and up to 50 W m^{-2} in some regions (Figure 16a). Ice cloud-dominated regions show the largest differences and are largely due to the ice cloud optical property differences. It is apparent that C51 considerably overestimates the ice CRE (Figure 16g). However, LW C6–C51 CRE differences are relatively small (approximately −1.00 W m^{-2} globally), although a reduction of LW CRE in C6 is apparent in the marine stratocumulus regions and over high-latitude southern oceans. From this comparison, we find that the C6 cloud product and optical property parameterization show much more consistent performance compared to CERES EBAF than the C51 counterparts.

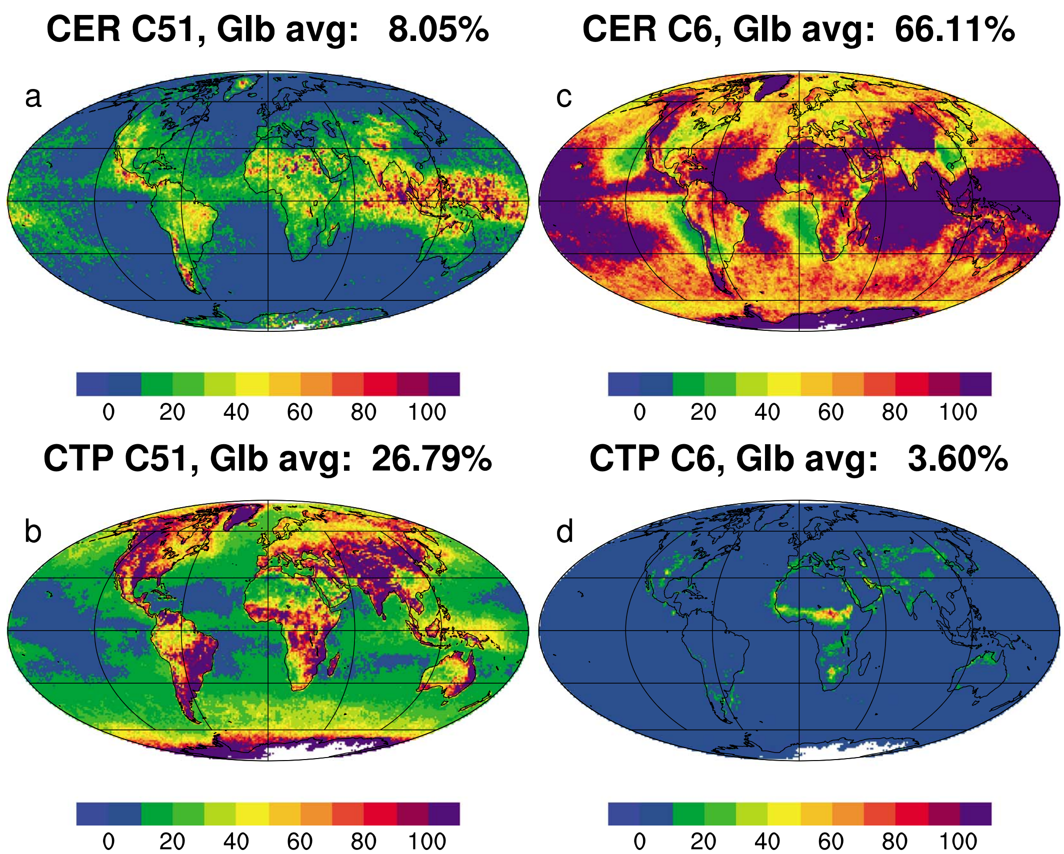

Figure 14. The relative difference between case 1 and case 2 in the number of valid pixels included in the aggregation for liquid water cloud: (a) CER C51, (b) CTP C51, (c) CER C6, and (d) CTP C6.

The CRE differences include the contribution from the cloud product differences as well as from the optical property parameterization differences. The differences in the SW and LW spectrum ranges in the CERES EBAF product and the RRTMG simulations are partially responsible for the discrepancies in the CRE. But most importantly, cloud types other than ice and liquid water clouds (e.g., mixed phase clouds) are excluded from this study but contribute to an unknown portion of the total CRE. In addition, the comparison between our simulations and the CERES EBAF products is rough and should be viewed with caution because they undergo different sampling and filtering processes which may affect the results. This topic is explored in more detail in a companion study [i.e., *Yi et al*., 2017].

5. Summary

In this study, we compare the collection 5.1 and collection 6 cloud physical (i.e., CTP, CTT, and CF) and optical (i.e., CER, COT, and CWP) properties retrieved from Aqua MODIS observations in 2012. The objective is to determine what differences emerged during the data collection change for the general users of the MODIS ice and liquid water cloud products. The differences are important as they are shown to have a significant impact on cloud radiative effect calculations. The C6 to C51 comparisons are based on examination of two cases: (1) when cloud retrievals are valid simultaneously in both C51 and C6 and (2) when all valid cloud retrievals are considered in their respective collections. The selected pixels for each day in 2012 are first aggregated and gridded in daily half-degree resolution equal-angle grid boxes and then further averaged annually, zonally, and globally considering the cloudy pixel numbers as the weighting factor.

From the ice cloud comparisons in case 1, systematic increases are found in the C6 CER of about 6.68 μm globally. Spatial differences in CER also contribute to differences in the variation of zonal averaged values.

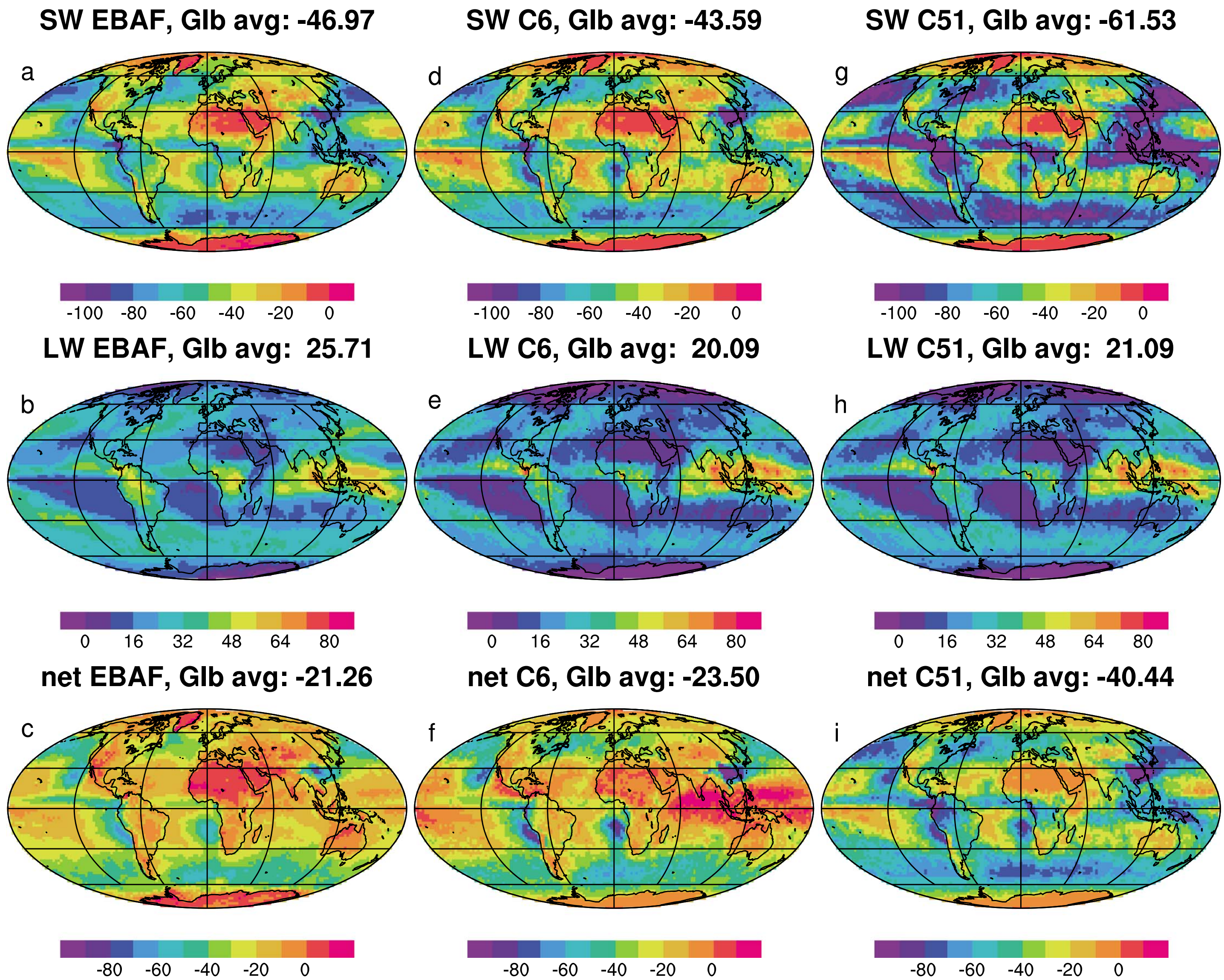

Figure 15. The 2012 annual averaged TOA SW, LW, and net total cloud radiative effects (unit: W m^{-2}) from the (a–c) CERES EBAF, (d–f) RRTMG simulation for C6, and (g–i) RRTMG simulation for C51.

The C51 COT is globally larger than the C6 COT by about 25%. The CER and COT changes tend to offset each other so that the C51 and C6 ice CWP are quite similar. Such C6–C51 differences can be largely attributed to the changes in ice cloud particle models from an ice habit mixture with smooth surfaces (collection 5) to a severely roughened aggregate of solid columns (collection 6) [*Platnick et al.*, 2017]. Comparison of the ice cloud pixels identified in both C51 and C6 not only highlights the impact of changing the ice cloud particle model but also illustrates the significant land-ocean differences, particularly in CWP and to a lesser degree, in CER. Consideration of all of the pixels in each collection (case 2) masks these land-ocean differences, emphasizing the need for both comparisons. There appears to be some compensating effects when all ice clouds are considered in their respective collections (case 2), likely due to the C6 changes in the cloud thermodynamic phase determination and the handling of optically thin cirrus. The ice cloud top properties, however, are mostly unchanged in the transition from C51 to C6. While there are negligible differences in the global averages, there are still some noticeable regional variations. Larger C6–C51 differences in ice CF are found over high latitudes.

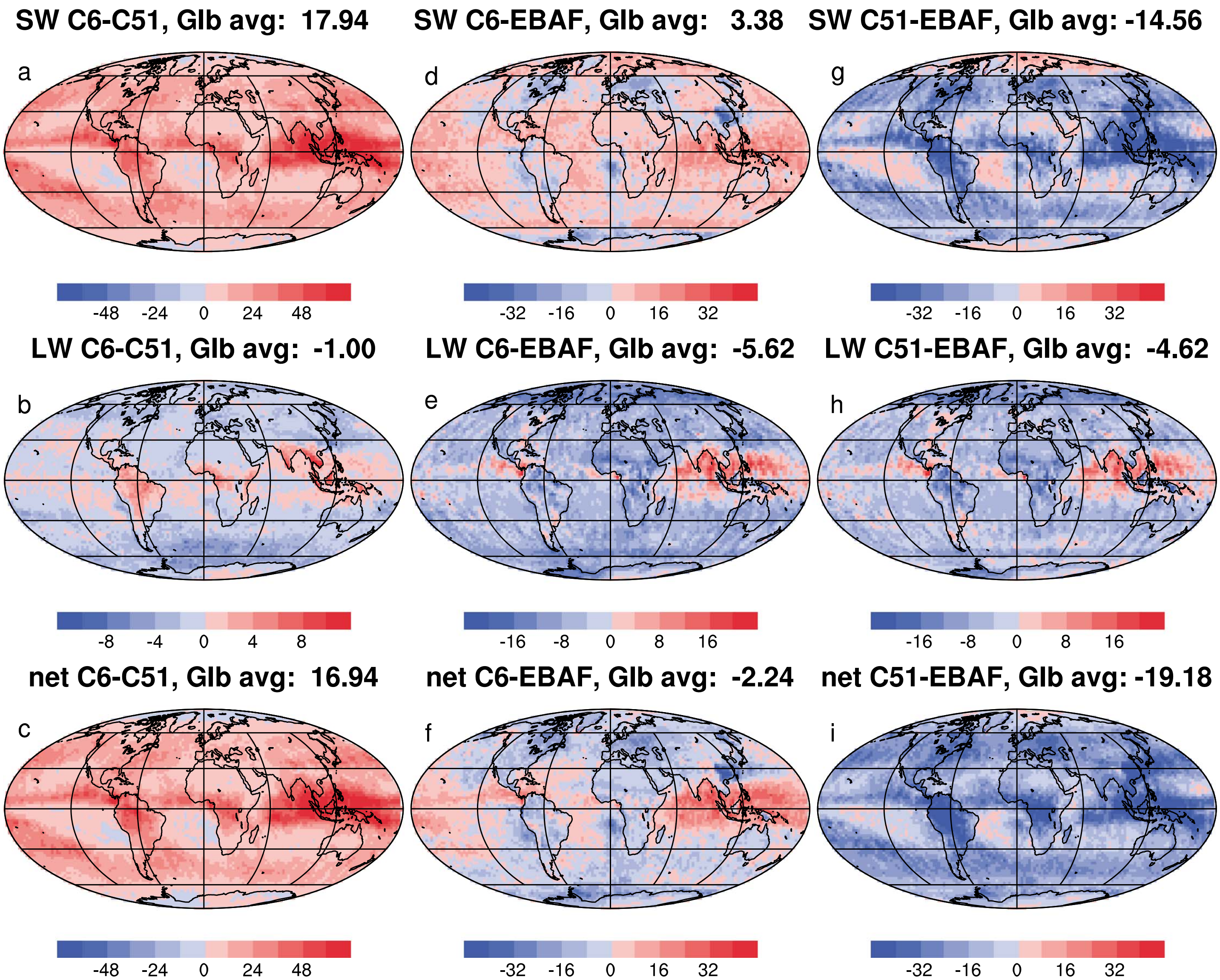

Figure 16. Differences of 2012 annual averaged TOA SW, LW, and net total cloud radiative effects (unit: W m^{-2}) (a–c) between C6 and C51 simulations, (d–f) between C6 and EBAF, and (g–i) between C51 and EBAF.

For liquid water clouds in case 1, there is generally good agreement between C51 and C6 for the optical properties, except for the high-latitude regions where there are fewer liquid water clouds. The CTP and CTT, however, show consistent decreases over land and tropical oceans, which indicates the higher and colder cloud tops in C6. In regions of more homogeneous cloud cover over subtropical and extratropical oceans, CTPs are considerably higher (40–80 hPa) and the CTTs are slightly cooler in C6. *Holz et al.* [2008] showed consistent 1–2 km biases of low cloud top heights in stratocumulus regions in MODIS C51 compared to CALIPSO lidar observations. The changes in CTP and CTT in C6 over ocean are the result of implementation of an IR window lapse rate method that mitigates the impact of the frequent inversions present in regions of persistent low-level liquid water clouds [*Baum et al.*, 2012].

By comparing cases 1 and 2, we determine whether case 1 is representative of the whole data set. Although more valid pixels are included in both C51 and C6 for ice clouds, there are only marginal differences between case 1 and case 2 parameters. The additional pixels are likely due to reduced cloud detection thresholds which increases the sensitivity to optically thin cirrus, as well as use of emissivity ratios of different IR channel pairs to improve cloud phase sensitivity and phase detection in thin cirrus clouds [*Baum et al*., 2012; *Heidinger and Pavolonis*, 2009; *Pavolonis*, 2010].

In case 2 liquid water clouds, greater than 66% more liquid water cloud pixels yield not only larger CER but also a much greater C6–C51 difference in CWP. These additional pixels in C6 can be partly attributed to the improved thermodynamic phase algorithm, which significantly increased the number of clouds identified as liquid water in C6. The use of the new 1 km cloud top pressures in C6, rather than the 5 km parameter in C51, as input to the optical property retrieval also increases the number of valid retrievals in regions where clouds are more inhomogeneous, e.g., in the trade cumulus regions [*Platnick et al*., 2017]. Improvements to the cloud mask for enhancing detection of low clouds over ocean [*Baum et al*., 2012] may also be contributing to the large increase of liquid water cloud pixels in C6. The cloud top properties are also affected by the valid pixel number differences, with considerably larger decreases in CTP and CTT over land when all valid C6 pixels are included. Such large differences between the number of valid retrievals and the resultant impacts to comparisons of cloud properties between the two collections illustrate the need for careful attention to how the data are filtered and aggregated for such comparisons.

Finally, we compared the TOA annual averaged total cloud SW, LW, and net CRE for the C6 and the corresponding C6–C51 differences, with the CERES EBAF cloud radiative effect product. We find that the C6 cloud product and optical property parameterization show much better modeling performance than the C51 counterparts.

6. Concluding Remarks

As our results are based on analysis of 1 year (2012) of the total Aqua MODIS cloud retrieval data set, the results may not be representative of other years. In general, we expect the changes from C51 to C6 in the ice and liquid water cloud products in other years to be consistent with these findings. Further detailed analysis is needed to explore all the various reasons underlying the changes shown here and may be useful in future improvements to the cloud retrieval effort. The observed changes are also expected to influence the radiative impacts of ice and liquid water clouds. For example, the increased ice cloud effective particle size may contribute to a decreased cloud radiative forcing at the top of the atmosphere. A more detailed analysis of the radiative impacts of C6–C51 differences in cloud properties is provided in a companion study.

Acknowledgments
The authors acknowledge the support from NASA grant NNX13AG91G (Rapp), NASA grants NNX14AP65A and NNX14AN48G (Baum), and a subcontract (award 629K996) from the University of Wisconsin (Yang). The Aqua MODIS level-2 collection 5.1 and collection 6 products were downloaded from the NASA Goddard Space Flight Center Level 1 and Atmosphere Archive and Distribution System, which is publicly available at https://ladsweb.nascom.nasa.gov/data/. The CERES EBAF data can be downloaded at http://ceres.larc.nasa.gov/order_data.php.

References

Ackerman, S. A., K. I. Strabala, W. P. Menzel, R. A. Frey, C. C. Moeller, and L. E. Gumley (1998), Discriminating clear sky from clouds with MODIS, *J. Geophys. Res.*, *103*, 32,141–32,157, doi:10.1029/1998JD200032.

Ackerman, S. A., R. E. Holz, R. Frey, E. W. Eloranta, B. Maddux, and M. McGill (2008), Cloud detection with MODIS. Part II: Validation, *J. Atmos. Ocean. Technol.*, *25*, 1073–1086.

Baum, B. A., P. Yang, A. J. Heymsfield, S. Platnick, M. D. King, and S. T. Bedka (2005), Bulk scattering models for the remote sensing of ice clouds. Part 2: Narrowband models, *J. Appl. Meteorol.*, *44*, 1896–1911.

Baum, B. A., W. P. Menzel, R. A. Frey, D. Tobin, R. E. Holz, S. A. Ackerman, A. K. Heidinger, and P. Yang (2012), MODIS cloud top property refinements for collection 6, *J. Appl. Meteorol. Climatol.*, *51*, 1145–1163.

Baum, B. A., P. Yang, A. J. Heymsfield, A. Bansemer, A. Merrelli, C. Schmitt, and C. Wang (2014), Ice cloud bulk single-scattering property models with the full phase matrix at wavelengths from 0.2 to 100 μm, *J. Quant. Spectrosc. Radiant. Transfer*, *146*, 123–139.

Dee, D. P., et al. (2011), The ERA-Interim reanalysis: Configuration and performance of the data assimilation system, *Q. J. R. Meteorol. Soc.*, *137*, 553–597, doi:10.1002/qj.828.

Delanoë, J., and R. J. Hogan (2010), Combined CloudSat-CALIPSO-MODIS retrievals of the properties of ice clouds, *J. Geophys. Res.*, *115*, D00H29, doi:10.1029/2009JD012346.

Foster, M. J., and A. Heidinger (2013), PATMOS-x: Results from a diurnally corrected 30-year cloud climatology, *J. Clim.*, *26*, 414–425.

Frey, R. A., S. A. Ackerman, Y. Liu, K. I. Strabala, H. Zhang, J. Key, and X. Wang (2008), Cloud detection with MODIS, Part I: Recent improvements in the MODIS cloud mask, *J. Atmos. Ocean. Technol.*, *25*, 1057–1072.

Heidinger, A. K., and M. J. Pavolonis (2009), Gazing at cirrus clouds for 25 years through a split window. Part I: Methodology, *J. Appl. Meteorol. Climatol.*, *48*, 1100–1116.

Heidinger, A. K., W. C. Straka, C. C. Molling, J. T. Sullivan, and X. Q. Wu (2010), Deriving an inter-sensor consistent calibration for the AVHRR solar reflectance data record, *Int. J. Remote Sens.*, *31*, 6493–6517.

Heidinger, A. K., M. J. Foster, A. Walther, and X. Zhao (2014), The pathfinder atmospheres-extended AVHRR climate dataset, *Bull. Am. Meteorol. Soc.*, *95*(6), 909–922.

Holz, R. E., S. A. Ackerman, F. W. Nagle, R. Frey, S. Dutcher, R. E. Kuehn, M. Vaughan, and B. A. Baum (2008), Global MODIS cloud detection and height evaluation using CALIOP, *J. Geophys. Res.*, *113*, D00A19, doi:10.1029/2008JD009837.

Holz, R. E., et al. (2016), Resolving ice cloud optical thickness biases between CALIOP and MODIS using infrared retrievals, *Atmos. Chem. Phys.*, *16*, 5075–5090.

Hong, G., P. Yang, B-C. Gao, B. A. Baum, Y. X. Hu, M. D. King, and S. Platnick (2007), High cloud properties from three years of MODIS Terra and Aqua data over the tropics, *J. Appl. Meteorol. Climatol.*, *46*, 1840–1856.

Hu, Y., and K. Stamnes (1992), An accurate parameterization of the radiative properties of water clouds suitable for use in climate models, *J. Clim.*, *6*, 728–742.

Iacono, M. J., J. S. Delamere, E. J. Mlawer, M. W. Shephard, S. A. Clough, and W. D. Collins (2008), Radiative forcing by long-lived greenhouse gases: Calculations with the AER radiative transfer models, *J. Geophys. Res.*, *113*, D13103, doi:10.1029/2008JD009944.

Jiang, J. H., H. Su, C. Zhai, S. T. Massie, M. R. Schoeberl, P. R. Colarco, S. Platnick, Y. Gu, and K. N. Liou (2011), Influence of convection and aerosol pollution on ice cloud particle effective radius, *Atmos. Chem. Phys.*, *11*, 457–463.

Jiang, J. H., et al. (2012), Evaluation of cloud and water vapor simulations in CMIP5 climate models using NASA "A-train" satellite observations, *J. Geophys. Res.*, *117*, D14105, doi:10.1029/2011JD017237.

Kaufman, Y. J., I. Koren, L. A. Remer, D. Rosenfeld, and Y. Rudich (2005), The effect of smoke, dust, and pollution aerosol on shallow cloud development over the Atlantic Ocean, *Proc. Natl. Acad. Sci. U.S.A.*, *102*, 11,207–11,212.

King, M., S. Platnick, W. P. Menzel, S. A. Ackerman, and P. A. Hubanks (2013), Spatial and temporal distribution of clouds observed by MODIS onboard the Terra and Aqua satellites, *IEEE Trans. Geosci. Remote Sens.*, *51*, 3826–3852, doi:10.1109/TGRS.2012.2227333.

King, M. D., W. P. Menzel, Y. J. Kaufman, D. Tanré, B. C. Gao, S. Platnick, S. A. Ackerman, L. A. Remer, R. Pincus, and P. A. Hubanks (2003), Cloud and aerosol properties, precipitable water, and profiles of temperature and humidity from MODIS, *IEEE Trans. Geosci. Remote Sens.*, *41*, 442–458.

King, M. D., S. Platnick, G. Wind, G. T. Arnold, and R. T. Dominguez (2010), Remote sensing of the radiative and microphysical properties of clouds during TC^4: Results from MAS, MASTER, MODIS, and MISR, *J. Geophys. Res.*, *115*, D00J07, doi:10.1029/2009JD013277.

Lebsock, M. D., G. L. Stephens, and C. Kummerow (2008), Multisensor satellite observations of aerosol effects on warm clouds, *J. Geophys. Res.*, *113*, D15205, doi:10.1029/2008JD009876.

Marchant, B., S. Platnick, K. Meyer, G. T. Arnold, and J. Riedi (2016), MODIS collection 6 shortwave-derived cloud phase classification algorithm and comparisons with CALIOP, *Atmos. Meas. Tech.*, *9*, 1587–1599.

Menzel, W. P., R. A. Frey, H. Zhang, D. P. Wylie, C. C. Moeller, R. E. Holz, B. Maddux, B. A. Baum, K. I. Strabala, and L. E. Gumley (2008), MODIS global cloud-top pressure and amount estimation: Algorithm description and results, *J. Appl. Meteorol. Climatol.*, *47*, 1175–1198.

Menzel, W. P., R. A. Frey, E. E. Borbas, B. A. Baum, G. Cureton, and N. Bearson (2016), Reprocessing of HIRS satellite measurements from 1980 to 2015: Development toward a consistent decadal cloud record, *J. Appl. Meteorol. Clim.*, *55*, 2397–2410, doi:10.1175/JAMC-D-16-0129.1.

Meyer, K., P. Yang, and B.-C. Gao (2007), Tropical ice cloud optical depth, ice water path, and frequency fields inferred from the MODIS level-3 data, *Atmos. Res.*, *85*, 171–182.

Oreopoulos, L., N. Cho, D. Lee, S. Kato, and G. J. Huffman (2014), An examination of the nature of global MODIS cloud regimes, *J. Geophys. Res. Atmos.*, *119*, 8362–8383, doi:10.1002/2013JD021409.

Pavolonis, M. J. (2010), Advances in extracting cloud composition information from spaceborne infrared radiances—A robust alternative to brightness temperatures. Part I: Theory, *J. Appl. Meteorol. Climatol.*, *49*, 1992–2012.

Platnick, S., M. D. King, S. A. Ackerman, W. P. Menzel, B. A. Baum, J. C. Riedi, and R. A. Frey (2003), The MODIS cloud products: Algorithms and examples from Terra, *IEEE Trans. Geosci. Remote Sens.*, *41*, 459–473.

Platnick, S., et al. (2015), MODIS cloud optical properties: User guide for the collection 6 level-2 MOD06/MYD06 product and associated level-3 datasets. Version 1.0, 141pp. [Available at http://modis-atmos.gsfc.nasa.gov/_docs/C6MOD06OPUserGuide.pdf.]

Platnick, S., et al. (2017), The MODIS cloud optical and microphysical products: Collection 6 updates and examples from Terra and Aqua, *IEEE Trans. Geosci. Remote Sens.*, *55*, 502–525, doi:10.1109/TGRS.2016.2610522.

Smith, N., W. P. Menzel, E. Weisz, A. K. Heidinger, and B. A. Baum (2013), A uniform space–time gridding algorithm for comparison of satellite data products: Characterization and sensitivity study, *J. Appl. Meteorol. Climatol.*, *52*, 255–268.

Stengel, M., A. Kniffka, J. F. Meirink, M. Lockhoff, J. Tan, and R. Hollmann (2014), CLAAS: The CM SAF cloud property data set using SEVIRI, *Atmos. Chem. Phys.*, *14*, 4297–4311.

Stephens, G. L., et al. (2008), CloudSat mission: Performance and early science after the first year of operation. *J. Geophys. Res.*, *113*, D00A18, doi:10.1029/2008JD009982.

Toller, G., X. Xiong, J. Sun, B. N. Wenny, X. Geng, J. Kuyper, A. Angal, H. Chen, S. Madhavan, and A. Wu (2013), Terra and Aqua moderate-resolution imaging spectroradiometer collection 6 level 1B algorithm, *J. Appl. Remote. Sens.*, *7(1)*, 073557, doi:10.1117/1.JRS.7.073557.

Waliser, D., et al. (2009), Cloud ice: A climate model challenge with signs and expectations of progress, *J. Geophys. Res.*, *114*, D00A21, doi:10.1029/2008JD010015.

Wang, C., P. Yang, B. A. Baum, S. Platnick, A. K. Heidinger, Y. Hu, and R. E. Holz (2011), Retrieval of ice cloud optical thickness and effective particle size using a fast infrared radiative transfer model, *J. Appl. Meteorol. Climatol.*, *50*, 2283–2297.

Winker, D. M., M. A. Vaughan, A. Omar, Y. X. Hu, K. A. Powell, Z. Liu, W. H. Hunt, and S. A. Young (2009), Overview of the CALIPSO mission and CALIOP data processing algorithms, *J. Atmos. Ocean. Technol.*, *26*, 2310–2323.

Wood, R., K. K. Comstock, C. S. Bretherton, C. Cornish, J. Tomlinson, D. R. Collins, and C. Fairall (2008), Open cellular structure in marine stratocumulus sheets, *J. Geophys. Res.*, *113*, D12207, doi:10.1029/2007JD009371.

Xiong, X., B. N. Wenny, and W. L. Barnes (2009), Overview of NASA Earth Observing Systems Terra and Aqua Moderate Resolution Imaging Spectroradiometer instrument calibration algorithms and on-orbit performance, *J. Appl. Remote. Sens.*, *3*, 032501, doi:10.1117/1.3180864.

Xiong, X., M. D. King, V. V. Salomonson, W. L. Barnes, B. N. Wenny, A. Angal, A. Wu, S. Madhavan, and D. O. Link (2016), Moderate Resolution Imaging Spectroradiometer on Terra and Aqua missions, in *Optical Payloads for Space Missions*, 1st ed., edited by S. E. Qian, pp. 53–89, John Wiley, Chichester, U. K.

Yang, P., L. Zhang, G. Hong, S. L. Nasiri, B. A. Baum, H.-L. Huang, M. D. King, and S. Platnick (2007), Differences between collection 4 and 5 MODIS ice cloud optical/microphysical products and their impact on radiative forcing simulations, *IEEE Trans. Geosci. Remote Sens.*, *45*, 2886–2899.

Yang, P., L. Bi, B. A. Baum, K. N. Liou, G. W. Kattawar, M. I. Mishchenko, and B. Cole (2013), Spectrally consistent scattering, absorption, and polarization properties of atmospheric ice crystals at wavelengths from 0.2 to 100 μm, *J. Atmos. Sci.*, *70*, 330–347.

Yang, P., K. N. Liou, L. Bi, C. Liu, B. Q. Yi, and B. A. Baum (2015), On the radiative properties of ice clouds: Light scattering, remote sensing, and radiation parameterization, *Adv. Atmos. Sci.*, *32*, 32–63.

Yi, B., P. Yang, B. A. Baum, T. L'Ecuyer, L. Oreopoulos, E. J. Mlawer, A. J. Heymsfield, and K. N. Liou (2013), Influence of ice particle surface roughening on the global cloud radiative effect, *J. Atmos. Sci.*, *70*, 2794–2807.

Yi, B., P. Yang, Q. Liu, P. van Delst, S. Boukabara, and F. Weng (2016), Improvements on the ice cloud modeling capabilities of the community radiative transfer model, *J. Geophys. Res. Atmos.*, *121*, 13,577–13,590, doi:10.1002/2016JD025207.

Yi, B., A. D. Rapp, P. Yang, B. A. Baum, and M. D. King (2017), A comparison of aqua MODIS ice and liquid water cloud physical and optical properties between collection 6 and collection 5.1: Cloud radiative effects, *J. Geophys. Res. Atmos.*, doi:10.1002/2016JD025654.

Zhang, G. J., A. M. Vogelmann, M. P. Jensen, W. D. Collins, and E. P. Luke (2010), Relating satellite-observed cloud properties from MODIS to meteorological conditions for marine boundary layer clouds, *J. Clim.*, *23*, 1374–1391.

Zhang, Z., P. Yang, G. W. Kattawar, J. Riedi, L.-C. Labonnote, B. A. Baum, S. Platnick, and H. L. Huang (2009), Influence of ice particle model on satellite ice cloud retrieval: Lessons learned from MODIS and POLDER cloud product comparison, *Atmos. Chem. Phys.*, *9*, 7115–7129.

Zhou, C., M. D. Zelinka, A. E. Dessler, and P. Yang (2013), An analysis of the short-term cloud feedback using MODIS data, *J. Clim.*, *26*, 4803–4815.